

# Actively variable-spectrum optoelectronics with black phosphorus

<https://doi.org/10.1038/s41586-021-03701-1>

Received: 22 January 2021

Accepted: 7 June 2021

Published online: 11 August 2021

 Check for updates

Hyungjin Kim<sup>1,2</sup>, Shiekh Zia Uddin<sup>1,2</sup>, Der-Hsien Lien<sup>1,2</sup>, Matthew Yeh<sup>1,2</sup>, Nima Sefidmooye Azar<sup>3</sup>, Sivacarendran Balendhran<sup>4</sup>, Taehun Kim<sup>1,2</sup>, Niharika Gupta<sup>1,2</sup>, Yoonsoo Rho<sup>5</sup>, Costas P. Grigoropoulos<sup>5</sup>, Kenneth B. Crozier<sup>3,4,6</sup> & Ali Javey<sup>1,2</sup>✉

Room-temperature optoelectronic devices that operate at short-wavelength and mid-wavelength infrared ranges (one to eight micrometres) can be used for numerous applications<sup>1–5</sup>. To achieve the range of operating wavelengths needed for a given application, a combination of materials with different bandgaps (for example, superlattices or heterostructures)<sup>6,7</sup> or variations in the composition of semiconductor alloys during growth<sup>8,9</sup> are used. However, these materials are complex to fabricate, and the operating range is fixed after fabrication. Although wide-range, active and reversible tunability of the operating wavelengths in optoelectronic devices after fabrication is a highly desirable feature, no such platform has been yet developed. Here we demonstrate high-performance room-temperature infrared optoelectronics with actively variable spectra by presenting black phosphorus as an ideal candidate. Enabled by the highly strain-sensitive nature of its bandgap, which varies from 0.22 to 0.53 electronvolts, we show a continuous and reversible tuning of the operating wavelengths in light-emitting diodes and photodetectors composed of black phosphorus. Furthermore, we leverage this platform to demonstrate multiplexed nondispersive infrared gas sensing, whereby multiple gases (for example, carbon dioxide, methane and water vapour) are detected using a single light source. With its active spectral tunability while also retaining high performance, our work bridges a technological gap, presenting a potential way of meeting different requirements for emission and detection spectra in optoelectronic applications.

The spectral range over which an optoelectronic device can operate is largely dictated by the bandgap of its photoactive material. To achieve the operating range needed for a given application, the bandgap is controlled either by constructing materials with varying alloy compositions, or by using complex structures consisting of materials with different bandgaps (for example, superlattices or heterostructure)<sup>10,11</sup>. While effective, these approaches come with increased complexity of fabrication, as they involve the precise control of material thickness and/or composition. In addition, these approaches produce devices whose ranges of operating wavelengths are fixed after fabrication. Although the absorption edge can be shifted by applying an electric field to produce a Franz–Keldysh effect or Stark effect<sup>12,13</sup>, the decrease in photoresponse and luminescence intensity at the extended spectral range, as well as the requirement for additional gate electrodes to apply the bias field, is a major bottleneck for developing tunable optoelectronics with high performance.

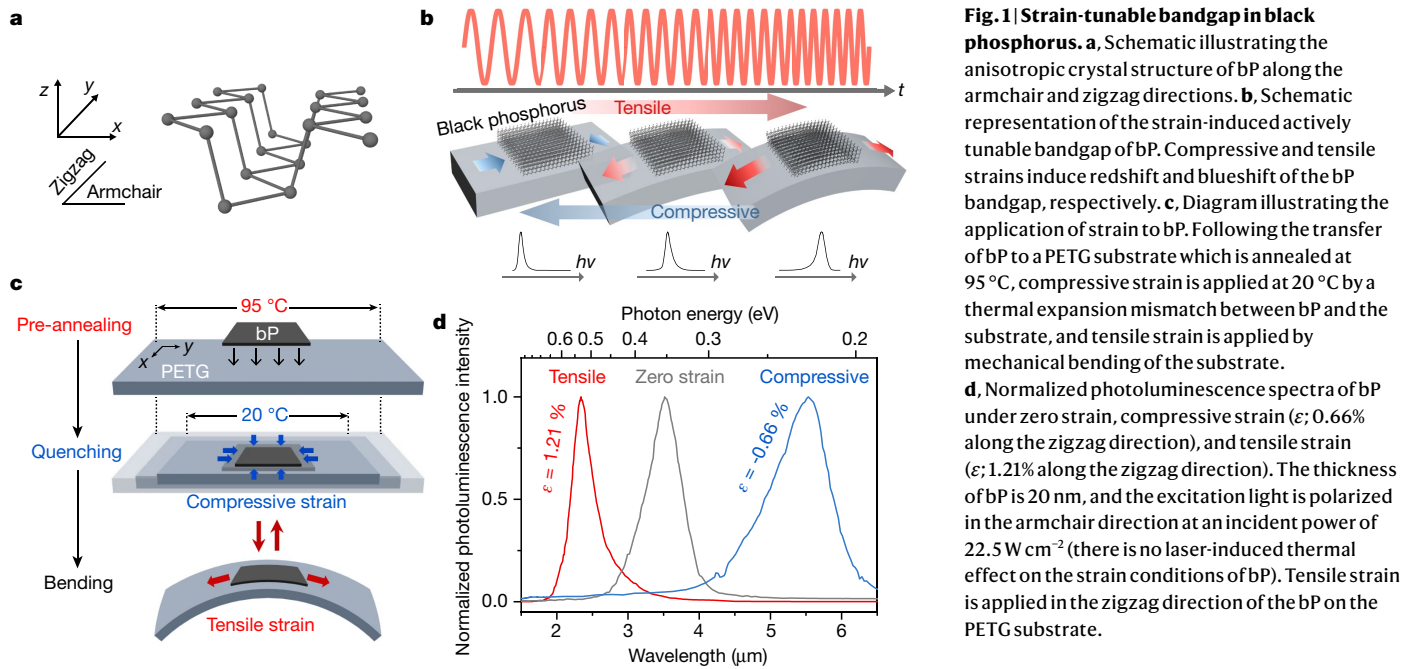
Strain is an effective knob with which to modulate the electronic and optical properties of semiconductors<sup>14–16</sup>, and can achieve reversible and controllable tuning of the bandgap. Although only a limited

amount of strain can be epitaxially applied in bulk crystalline materials, two-dimensional (2D) materials can sustain much larger elastic strain, thus allowing for wide tuning of their optical bandgap<sup>17,18</sup>. Owing to its puckered lattice structure, black phosphorus (bP) has shown unique strain-dependent properties, including a bandgap that is highly sensitive to strain<sup>19–22</sup>, anomalous strain dependence of the bandgap<sup>23</sup>, tunable van der Waals interaction<sup>24</sup>, and piezoelectricity<sup>25</sup>. Strain can be applied in a reversible manner in bP owing to its membrane nature, which does not require a selective thinning and lift-off process<sup>26,27</sup>. The bandgap of multilayer bP also spans the portion of the infrared region in which there is a rapidly increasing demand for optical communications, thermal imaging, health monitoring, spectroscopy and gas sensing<sup>28</sup>. Moreover, the low Auger recombination velocity<sup>29,30</sup> and direct bandgap of bP at all thicknesses are advantageous for high-efficiency optoelectronic applications. However, despite considerable interest in developing actively tunable infrared optoelectronic devices, no substantial progress has been made in that direction.

Here we use the strain-tunable bandgap of bP to demonstrate actively variable-spectrum optoelectronic (AVSO) devices that operate in the

<sup>1</sup>Department of Electrical Engineering and Computer Sciences, University of California, Berkeley, CA, USA. <sup>2</sup>Materials Sciences Division, Lawrence Berkeley National Laboratory, Berkeley, CA, USA. <sup>3</sup>Department of Electrical and Electronic Engineering, University of Melbourne, Melbourne, Victoria, Australia. <sup>4</sup>School of Physics, University of Melbourne, Melbourne, Victoria, Australia.

<sup>5</sup>Department of Mechanical Engineering, University of California, Berkeley, CA, USA. <sup>6</sup>Australian Research Council (ARC) Centre of Excellence for Transformative Meta-Optical Systems (TMOS), University of Melbourne, Melbourne, Victoria, Australia. ✉e-mail: ajavey@berkeley.edu



infrared regime at room temperature. Covering 2.3  $\mu\text{m}$  to 5.5  $\mu\text{m}$ , the bP bandgap exhibits a modulation rate of 1.70  $\mu\text{m}^{-1}$  by strain using our methods—the highest value reported for direct bandgap semiconductors. This enables a wide modulation of its spectral range in both light-emitting and light-detecting devices at will, without sacrificing its performance. We also show continuous and reversible tuning of mid-wavelength infrared (MWIR) electroluminescence using a bP–MoS<sub>2</sub> heterostructure on a flexible substrate. We also extend the detection range of highly responsive bP photodetectors by applying strain. Finally, we detect multiple gases (such as CO<sub>2</sub>, CH<sub>4</sub> and H<sub>2</sub>O) using a single tunable infrared light source. Owing to its reversibility and capacity for active spectral tunability while retaining high performance, our approach provides versatility in various fields in which a tunable spectrum is required at room temperature.

### Strain-tunable bandgap in bP

Black phosphorus has a puckered hexagonal structure with two crystal orientations in each layer: ‘armchair’ (in the x direction) and ‘zigzag’ (in the y direction) (Fig. 1a). The strain-induced actively variable bandgap of bP should enable AVSO devices at room temperature that exhibit a wide and reversible tunability of operating wavelength (Fig. 1b). We transferred mechanically exfoliated bP onto a pre-annealed polyethylene terephthalate glycol modified (PETG) substrate at 95 °C (Fig. 1c). Rapid thermal quenching of the bP–PETG sample to room temperature resulted in the application of compressive strain to bP due to the coefficient of thermal expansion (CTE) mismatch between bP and PETG (see Methods). Thereafter, we applied tensile strain by bending the sample. Here we quantify the strain via its zigzag (y)-direction component (Extended Data Fig. 1a, b). Therefore, we determined the strain in bP from the sum of the compressive (negative) strain in the zigzag direction induced by the thermal expansion mismatch, and the tensile (positive) strain in the zigzag direction from bending stress.

We verified the strain-induced bandgap shift in bP by infrared photoluminescence spectroscopy (Fig. 1d). Before bending, the photoluminescence peaked at a wavelength of 5.5  $\mu\text{m}$  (0.66%; compressive). We observed a large spectral blueshift of 3.2  $\mu\text{m}$  after mechanical bending (1.21%; tensile), corresponding to a bandgap shift from 0.22 eV to 0.53 eV induced by applied strain. At a strain of 0%, the photoluminescence had

a peak position at 0.35 eV, which is in good agreement with the photoluminescence spectrum of unstrained bP from the literature<sup>31</sup>. Moreover, Raman studies showed that the rates of shifting induced by the applied strain were consistent with previous reports<sup>25,32</sup> (Extended Data Fig. 1c–e). In addition, we found that built-in compressive strain plays a major part in preventing any partial relaxation or slippage during bending, retaining up to 1.21% of tensile strain (Extended Data Fig. 2a). Owing to the effective transfer of mechanical strain and extraordinary sensitivity of the bandgap to strain, our method offers a broad and continuous range of bandgap tuning at room temperature. The wavelength range spanned by our approach is from the short-wavelength infrared (SWIR) to the MWIR and could otherwise be accessed only by several devices comprising bulk semiconductor alloys with different compositions.

We carried out detailed optical characterization using infrared photoluminescence (IRPL) spectroscopy to further investigate the tunability of the bandgap in bP using strain. As the strain increased, so too did the photoluminescence intensity, and the wavelength of the spectral peak varied continuously from 5.5  $\mu\text{m}$  to 2.3  $\mu\text{m}$  (Fig. 2a). The blueshift rate of the bP bandgap induced by strain was 1.70  $\mu\text{m}^{-1}$  (162 meV $^{-1}$ ), which is substantially higher than that of other semiconductors with similar bandgaps (for example, Ge and InAs) (Fig. 2b and Extended Data Table 1). Changing the direction of tensile strain with respect to the crystal orientation of bP (armchair or zigzag) did not have a large effect on the magnitude of the bandgap shift (Extended Data Fig. 2c), in agreement with previous work<sup>22</sup>. Additionally, light absorption at the photoluminescence excitation wavelength showed little dependence on strain (Extended Data Fig. 2d). The relative photoluminescence quantum yield in bP under different strains is thus given by the integrated luminous intensity divided by the incident power as well as by light absorption (Fig. 2c). Strained bP exhibited a continuous increase in photoluminescence quantum yield in the high-pump regime, whereas in unstrained bP the quantum yield remained constant. Because our range of incident power is less than two orders of magnitude (limited by the measurement setup), it is not sufficient to extract recombination coefficients by fitting the incidence-power-dependent data we have. This introduces uncertainty in determining which of the parameters (Shockley–Read–Hall (SRH), radiative or Auger) is affected by strain, with respect to carrier densities. The photoluminescence quantum yield in bP under tensile strain (1.21%) is higher than that in bP under

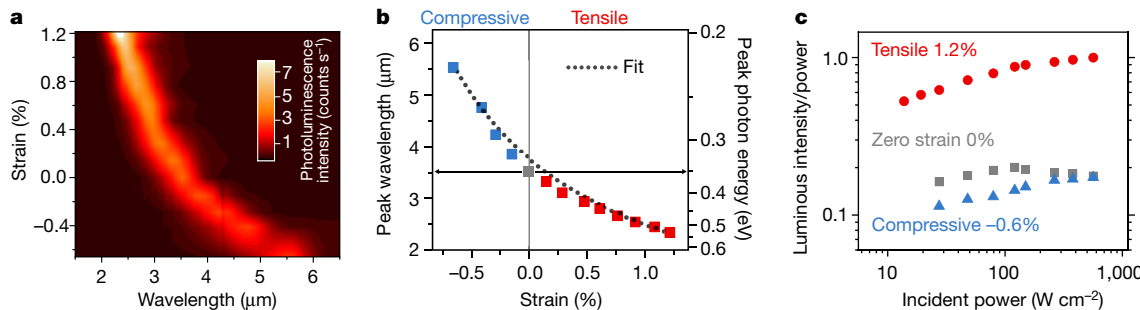


**Fig. 2 | Strain-induced modification of the bandgap in bP.**

**a**, Photoluminescence spectra of bP as a function of strain along the zigzag (*y*) direction. **b**, Strain-dependent shift in the photoluminescence spectral peak in bP. The fit indicates that the peak modulation rate is a wavelength shift of 1.70  $\mu\text{m}$  per cent of strain, covering 5.5  $\mu\text{m}$  to 2.3  $\mu\text{m}$ . Laser-induced thermal effects on strain are precluded by using a low excitation power, where the photoluminescence spectral peak remains constant as laser power density

increases (Extended Data Fig. 2b). **c**, Integrated photoluminescence intensity normalized by incident power as a function of power density for bP under different strain conditions. In all of these measurements, the bP thickness is 20 nm and the substrate is PETG. We also showed reversible and repeatable bandgap tuning, indicating that there is no mechanical slip between bP and the substrate over multiple cycles (Extended Data Fig. 2e).

compressive strain (0.66%) and unstrained bP. These results can be attributed to the change in effective mass by strain. Namely, the uniaxial tensile strain strongly alters the effective mass, with a blueshift of the bandgap and an increase in the radiative recombination rate. As operation at high current density is required in light-emitting devices, this property makes bP under tensile strain a suitable material for high-efficiency infrared-light-emitting devices.

### Strain-tunable MWIR light emission

Recently, an electrically pumped emission from bP has shown great promise as a light source at MWIR wavelengths<sup>33–35</sup>, owing to its direct bandgap even in bulk limit and its low Auger recombination velocity<sup>29,30</sup>. By leveraging the ability to widely modulate the bandgap of bP through strain, we developed strain-tunable light-emitting diodes (LEDs) based on bP–MoS<sub>2</sub> heterojunctions (Fig. 3a, b), with tensile strain applied through bending along the zigzag orientation of bP (Fig. 3c). We used MoS<sub>2</sub> as an electron-selective contact, and polyimide as the substrate, because PETG cannot withstand conventional lithography processes (see Methods). As we varied strain from compressive to tensile, the peak in the electroluminescence spectrum shifted continuously from 4.07  $\mu\text{m}$  (0.20%; compressive) to 2.70  $\mu\text{m}$  (1.06%; tensile) (Fig. 3d). Similar to the trend observed in our photoluminescence results, the electroluminescence intensity also increased with tensile strain as the emission wavelength became shorter. We characterized the peak wavelength of the electroluminescence as a function of the current density for different densities (Extended Data Fig. 3a). We also simulated the angular intensity distributions of the bP LED at two emission wavelengths (4.07  $\mu\text{m}$  and 2.70  $\mu\text{m}$ ), which were found to be similar (Extended Data Fig. 3b, c). We observed that, at all current densities, the bP LED under tensile strain showed higher electroluminescence intensity than when in compressive strain (Fig. 3e). The enhancement in electroluminescence with tensile strain was due to the enhancement in photoluminescence quantum yield, as the injection efficiency did not improve with strain (Extended Data Fig. 3d). The light emission from the bP LED was highly polarized, consistent with previous reports<sup>33–35</sup> (Fig. 3e, inset). Our bP LED also showed stable tunability of the emission wavelength above room temperature (between 20 °C and 100 °C; Extended Data Fig. 4). However, the emission intensity decreased with increasing temperature, which can be attributed to the thermal activation of the nonradiative recombination centres at high temperatures<sup>31</sup>. We extracted the internal quantum efficiency (IQE) of our bP LED, which is plotted along with the theoretical photoluminescence quantum yield of InAs, PbSe, GaSb and bP as a function of carrier concentration in Fig. 3f. Our device showed a peak IQE of 0.73% (0.2%; compressive)

and 2.47% (1.0%; tensile) at room temperature. A detailed discussion of measuring output power to calculate the IQE of the bP LED is provided in the Methods. For the case of a semiconductor with low background doping (that is, where  $n = p$ ), the theoretical photoluminescence quantum yield is calculated according to a standard ABC recombination model as:

$$\text{QY} = \frac{B(n^2 - n_i^2)}{\frac{A(n^2 - n_i^2)}{n} + B(n^2 - n_i^2) + 2Cn(n^2 - n_i^2)}$$

where QY is the quantum yield;  $n_i$  is the intrinsic carrier concentration; and  $A$ ,  $B$  and  $C$  are the SRH, radiative and Auger recombination coefficients, respectively. The parameters for InAs, PbSe, GaSb and bP used to calculate quantum yield are summarized in Extended Data Table 1. As the SRH recombination coefficient is an extrinsic parameter and highly dependent on material quality, we assumed it to be zero for this analysis. For small-bandgap semiconductors, the Auger recombination is likely to be pronounced and a limiting factor for LED performance. This originates from the relationship between the ratio of the Auger lifetime ( $\tau_a$ ) to the radiative lifetime ( $\tau_r$ ) and the bandgap ( $E_g$ ), which is given by:

$$\frac{\tau_a}{\tau_r} \propto \exp \left[ \left( \frac{\frac{m_e^*}{m_h^*}}{1 + \frac{m_e^*}{m_h^*}} \right) \left( \frac{E_g}{k_B T} \right) \right] \quad (1)$$

where  $m_e^*$  and  $m_h^*$  are the effective masses of electrons and holes, respectively;  $k_B$  is Boltzmann's constant; and  $T$  is temperature<sup>36,37</sup>. As  $m_e^*$  and  $m_h^*$  in bP have similar values, the effective mass ratio ( $m_e^*/m_h^*$ ) is much higher than that of other small-bandgap semiconductors. According to equation (1), this results in suppressed Auger recombination (a longer Auger lifetime), which leads to bP's theoretical quantum-yield limit being much higher than that of other small-bandgap semiconductors in the high-injection regime.

We characterized the cyclic repeatability and stability of emission tuning in our bP LED, revealing reversible and stable emission tuning over 500 bending cycles during roughly 6 h of operation (Fig. 3g, h and Supplementary Video 1). A light source capable of active and continuous tuning of its operating wavelength within this spectral region is of particular importance, as this wavelength range consists of various wavelength bands essential for gas detection and chemical analysis. Our strain-tunable bP LED not only provides a wide tuning capability that is equivalent to the integration of numerous devices made from bP with a thickness range of 7–200 nm, but also enhances the performance of MWIR light-emitting devices by applied strains. Furthermore, the

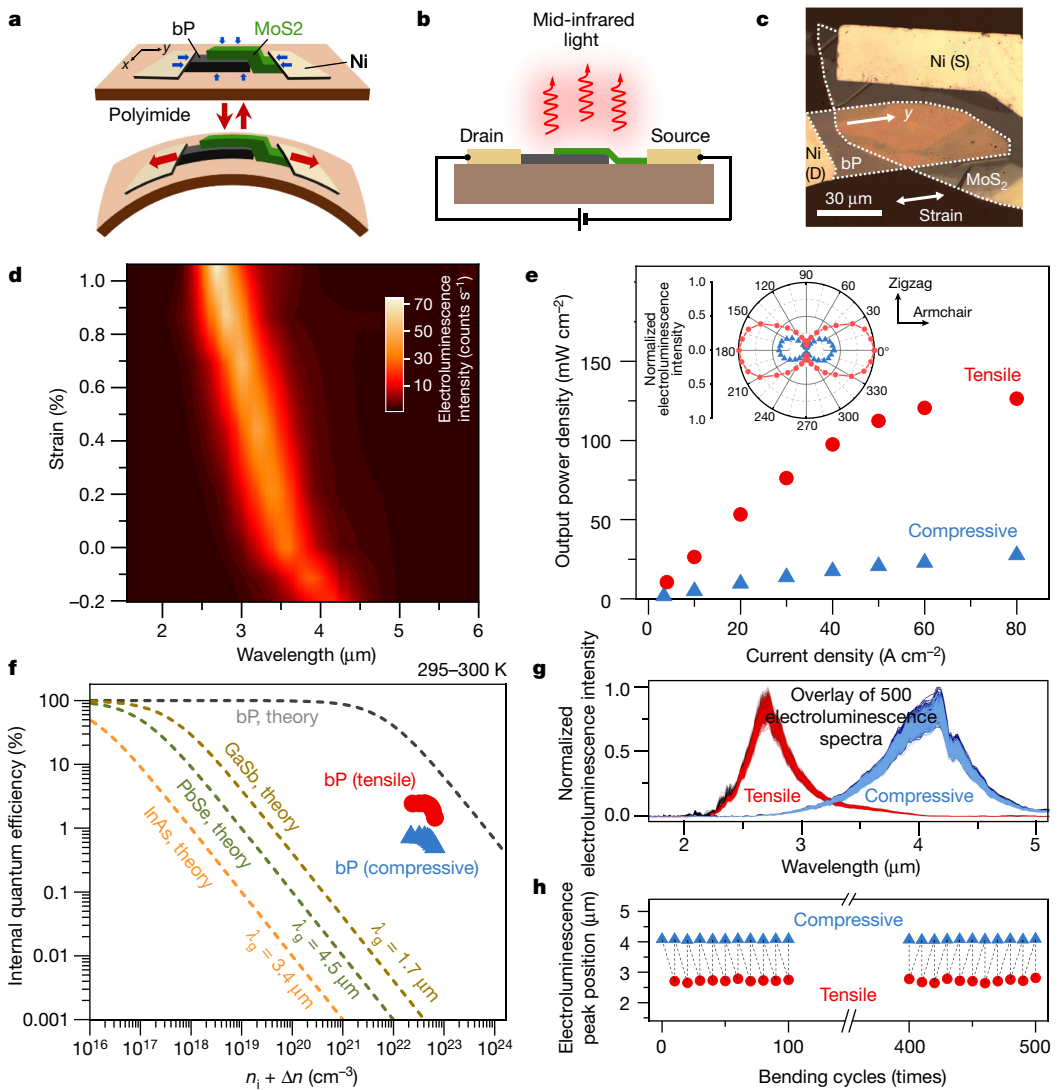


**Fig. 3 | Strain-tunable MWIR LEDs based on a bP–MoS<sub>2</sub> heterostructure.** **a**, Schematic showing a strain-tunable bP–MoS<sub>2</sub> LED. **b**, Schematic of the device architecture, showing MWIR electroluminescence under forward bias across the bP–MoS<sub>2</sub> heterojunction on a polyimide substrate. **c**, Optical micrograph of a representative device. **d**, Strain-dependent electroluminescence spectra. **e**, Light-current characteristics under 0.20% compressive or 1.06% tensile strain. Inset, normalized integrated electroluminescence intensity as a function of emission polarization angle. **f**, Theoretical internal quantum yield,

limited by Auger recombination, for InAs, PbSe, GaSb, and bP at room temperature, together with the measured internal quantum efficiency of the bP device shown in **e**.  $\lambda_g$ , bandgap wavelength. **g**, Overlay of 500 electroluminescence spectra and **h**, shift in the electroluminescence spectral peak observed in a bP LED, during 500 cycles of bending ( $1.06 \pm 0.05\%$ ; tensile) and relaxation (Supplementary Video 1). The thickness of the bP in the device is 20 nm, and all of the electroluminescence measurements were performed at a current density of  $20 \text{ A cm}^{-2}$ .

low operating power of our bP LEDs and their potential for monolithic integration with silicon technology<sup>35</sup> would be advantageous for numerous applications.

## Gas sensing with strain-tunable MWIR LEDs

Nondispersive infrared (NDIR) gas sensing has attracted great interest owing to its fast response and stable lifetime<sup>38</sup>. Thermal emitters (for example, tungsten filament lamps) are often used in NDIR gas sensors as light sources, but their slow modulation and high power consumption remain key challenges that make them disadvantageous for use in real-time gas-monitoring devices with extended lifetimes—a step towards the ‘Internet of Things’<sup>39,40</sup>. Strain-tunable bP LEDs with low operating power, fast modulation and rapid stabilization suggest a solution, permitting multiplexed gas detection with a single light source, where the emission wavelength can be tuned over a broad range to suit various target gases.

Our NDIR gas-sensing setup (Fig. 4a) and measurement process are detailed in the Methods. We varied the strain applied to our bP LED such that that the peak wavelength of the electroluminescence spectrum shifted to match the dominant absorption peaks of H<sub>2</sub>O, CH<sub>4</sub> and CO<sub>2</sub> (Extended Data Fig. 5a). As the emission spectrum of our bP LED under compressive strain has a large overlap with the absorption spectrum of CO<sub>2</sub> (Fig. 4b), the electroluminescence intensity from a bP LED measured by the detector at 4.3 μm was attenuated by CO<sub>2</sub> absorption, enabling detection over a wide range of CO<sub>2</sub> concentrations from 0.005% to 100% (Fig. 4d). On the other hand, under 0.3% tensile strain, CH<sub>4</sub> gas with a concentration range of 0.05% to 2.5% (50% of the lower explosive limit) was detected, resulting from attenuation of the measured electroluminescence intensity corresponding to CH<sub>4</sub> absorption at 3.3 μm (Fig. 4c, e). We also characterized the selectivity of gas sensing between CO<sub>2</sub> and CH<sub>4</sub> and the long-term stability of the setup (Extended Data Fig. 5b–e). We fit the electroluminescence intensity measured by the photodiode as a function of target gas

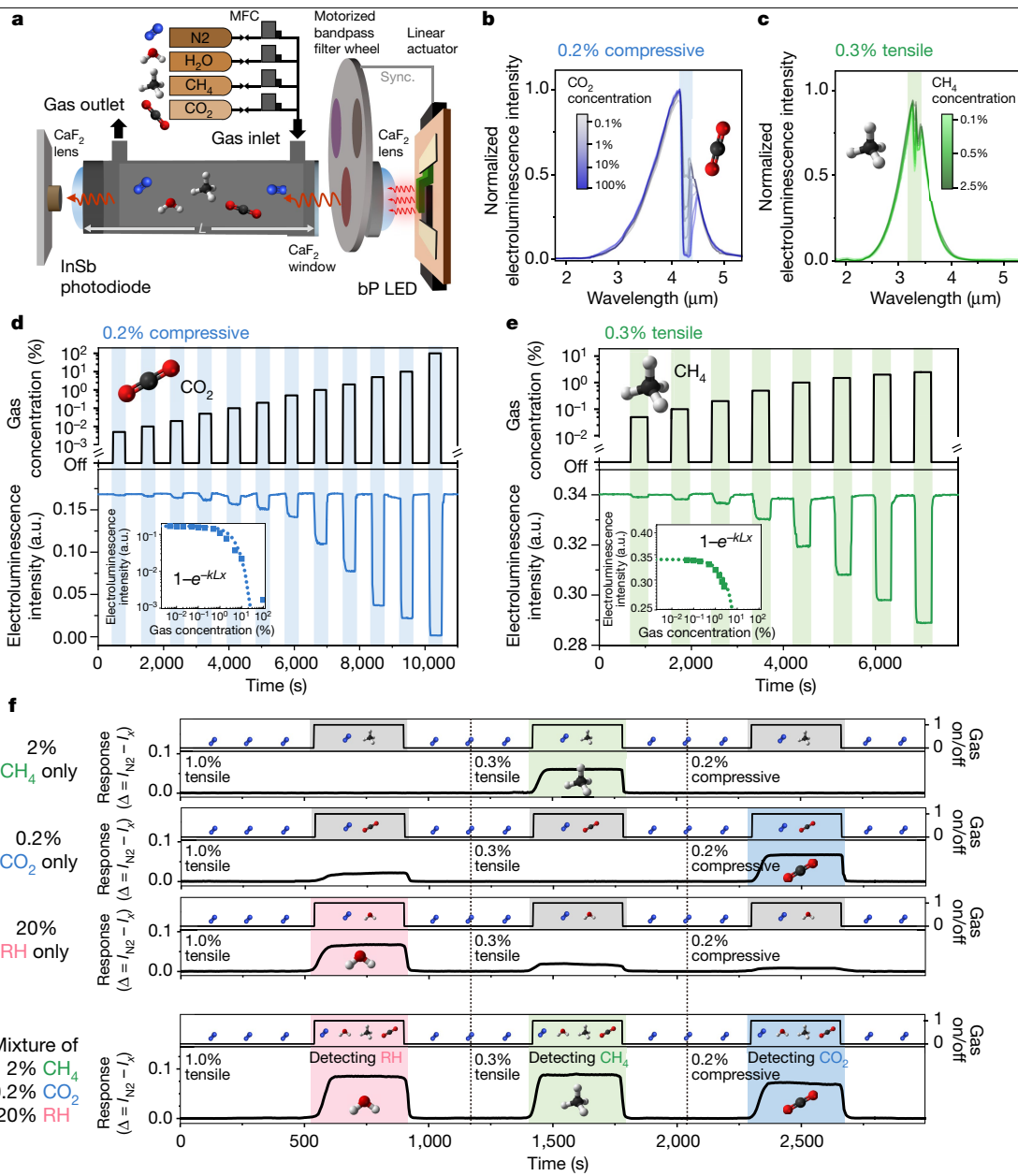


**Fig. 4 | NDIR gas sensing using strain-tunable LEDs.** **a**, Schematic diagram showing the NDIR gas-sensing system using a strain-tunable bP LED. MFC, mass flow controller. **b, c**, Normalized electroluminescence spectra of a bP LED (0.2%; compressive) in the presence of CO<sub>2</sub> gas (**b**) and a bP LED (0.3%; tensile) in the presence of CH<sub>4</sub> gas (**c**) at different concentrations. **d, e**, Sensor response characteristics of a bP LED (0.2%; compressive) at varying concentrations of CO<sub>2</sub> pulses (**d**) and a bP LED (0.3%; tensile) at varying concentrations of CH<sub>4</sub> pulses (**e**). Insets, data fit using a Beer–Lambert law model. **f**, Real-time

multiplexed sensing of individual target gases, from a gas mixture consisting of H<sub>2</sub>O (relative humidity (RH) 20%), CH<sub>4</sub> (2%), and CO<sub>2</sub> (0.2%), using a bP LED under 1.0% tensile, 0.3% tensile, and 0.2% compressive strain, respectively. Responses from individual gases (CH<sub>4</sub>, CO<sub>2</sub>, and H<sub>2</sub>O) were measured under different strains to characterize the selectivity of the multiplexed gas-sensing system. Note that the electroluminescence intensity (**d, e**) is the value recorded by the InSb photodiode on the opposite end of the gas cell.

concentrations using the modified Beer–Lambert law model, given by  $FA = (I_{N_2} - I_x)/I_{N_2} = 1 - \exp(-kLx)$ , where FA is the fractional absorbance of the target gas,  $I_{N_2}$  and  $I_x$  are the electroluminescence intensity measured by the photodiode under a nitrogen purge and at a target gas concentration of  $x$ , respectively;  $k$  is a fitting constant; and  $L$  is the chamber length (2") (Fig. 4d, e, inset). By leveraging the repeatable and continuous tuning capability of our strain-tunable bP LED, we showed multiplexed gas sensing (Fig. 4f). We measured responses from the individual gases (CH<sub>4</sub> only, CO<sub>2</sub> only, and water only) in order to characterize the selectivity of our multiplexed gas-sensing system. A sequence of responses from a mixed gas pulse consisting of 0.2% CO<sub>2</sub>, 2% CH<sub>4</sub> and H<sub>2</sub>O at 20% relative humidity indicates that H<sub>2</sub>O (1.0%

tensile strain), CH<sub>4</sub> (0.3% tensile strain) and CO<sub>2</sub> (0.2% compressive strain) can be detected with a single light source, by applying different strains to tune the peak emission wavelength of the bP LED.

### Strain-tunable photodetection

Photodetectors based on bP have been extensively studied<sup>41–48</sup>. Here, we applied the same concept to realize actively tunable photodetection with bP. We fabricated spectrally tunable bP-based photoconductors on a PETG substrate to apply strain (Extended Data Fig. 6a, b). As the tensile strain was applied in the zigzag orientation of bP (Extended Data Fig. 6c), the cutoff wavelength (the wavelength at which the

responsivity is 50% of the peak value) of the bP photoconductor was continuously tuned from  $4.32\text{ }\mu\text{m}$  (0.4%; compressive) to  $2.44\text{ }\mu\text{m}$  (1.0%; tensile) (Extended Data Fig. 6d). Our strain-tunable bP photoconductor showed a peak specific detectivity ( $D^*$ ) of  $5.97 \times 10^9\text{ cm Hz}^{1/2}\text{ W}^{-1}$  at  $\lambda = 4.0\text{ }\mu\text{m}$  (0.4%; compressive), and a peak  $D^*$  of  $8.45 \times 10^9\text{ cm Hz}^{1/2}\text{ W}^{-1}$  at  $\lambda = 2.0\text{ }\mu\text{m}$  (1.0%; tensile) (Extended Data Fig. 7c)—promising values among the commercially available photodetectors, especially for room-temperature operations. This suggests that our strategy can bridge the photodetection gap in the wavelength range between SWIR and MWIR. The strain-tunable bP photoconductor thus combines two benefits—high detectivity at room temperature and broadband tuning capability—arising from the highly strain-sensitive bP bandgap<sup>19–22</sup>. Detailed characterization and analysis of photodetection are provided in the Methods and Extended Data Figs. 6, 7.

## Conclusion

We have used the strain-tunable bandgap of bP to develop actively tunable infrared optoelectronic devices, including LEDs and photodetectors, at room temperature. The AVSO devices developed here have unprecedented versatility and thus important implications in fields such as optical communications, chemical sensing and spectroscopy, where a tunable spectrum is required. To this end, we demonstrated one such application of this tunable optoelectronic platform by performing multiplexed gas sensing with a single device. By expanding upon this approach, one could potentially explore the integration of devices on piezoelectric substrates or the use of micro-electromechanical systems (MEMS), although there are a number of processing challenges that need to be overcome. Furthermore, it may be possible to extend to long-wave infrared wavelengths by further increasing the amount of compressive strain applied to bP through substrate engineering. Our active strain-tuning scheme might also be applicable to other 2D materials, providing a path towards spectrally tunable optoelectronics across the electromagnetic spectrum.

## Online content

Any methods, additional references, Nature Research reporting summaries, source data, extended data, supplementary information, acknowledgements, peer review information; details of author contributions and competing interests; and statements of data and code availability are available at <https://doi.org/10.1038/s41586-021-03701-1>.

- Kahn, J. M. & Barry, J. R. Wireless infrared communications. *Proc. IEEE* **85**, 265–298 (1997).
- Vollmer, M. & Mollmann, K.-P. *Infrared Thermal Imaging: Fundamentals, Research and Applications* (2nd edn) (Wiley-VCH, Weinheim, 2018).
- Bagavathiappan, S., Lahiri, B. B., Saravanan, T., Philip, J. & Jayakumar, T. Infrared thermography for condition monitoring—a review. *Infrared Phys. Technol.* **60**, 35–55 (2013).
- Baker, M. J. et al. Using Fourier transform IR spectroscopy to analyze biological materials. *Nat. Protocols* **9**, 1771–1791 (2014).
- Gibson, D. & Macgregor, C. A novel solid state non-dispersive infrared CO<sub>2</sub> gas sensor compatible with wireless and portable deployment. *Sensors (Basel)* **13**, 7079–7103 (2013).
- Haugan, H. J., Szmulowicz, F., Brown, G. J. & Mahalingam, K. Bandgap tuning of InAs/GaSb type-II superlattices for mid-infrared detection. *J. Appl. Phys.* **96**, 2580–2585 (2004).
- Kang, J., Tongay, S., Zhou, J., Li, J. & Wu, J. Band offsets and heterostructures of two-dimensional semiconductors. *Appl. Phys. Lett.* **102**, 012111 (2013).
- Wu, J. et al. Universal bandgap bowing in group-III nitride alloys. *Solid State Commun.* **127**, 411–414 (2003).
- Ning, C.-Z., Dou, L. & Yang, P. Bandgap engineering in semiconductor alloy nanomaterials with widely tunable compositions. *Nat. Rev. Mater.* **2**, 17070 (2017).
- Yang, Z. et al. Single-nanowire spectrometers. *Science* **365**, 1017–1020 (2019).
- Kramer, I. J., Levina, L., Debnath, R., Zhitomirsky, D. & Sargent, E. H. Solar cells using quantum funnels. *Nano Lett.* **11**, 3701–3706 (2011).
- Whitney, W. S. et al. Field effect optoelectronic modulation of quantum-confined carriers in black phosphorus. *Nano Lett.* **17**, 78–84 (2017).
- Liu, Y. et al. Gate-tunable giant stark effect in few-layer black phosphorus. *Nano Lett.* **17**, 1970–1977 (2017).
- Yablonovitch, E. & Kane, E. O. Band structure engineering of semiconductor lasers for optical communications. *J. Lightwave Technol.* **6**, 1292–1299 (1988).
- Thompson, S. E. et al. A 90-nm logic technology featuring strained-silicon. *IEEE Trans. Electron Dev.* **51**, 1790–1797 (2004).
- Chen, Y. et al. Strain engineering and epitaxial stabilization of halide perovskites. *Nature* **577**, 209 (2020).
- Lee, C., Wei, X., Kysar, J. W. & Hone, J. Measurement of the elastic properties and intrinsic strength of monolayer graphene. *Science* **321**, 385–388 (2008).
- Bertolazzi, S., Brivio, J. & Kis, A. Stretching and breaking of ultrathin MoS<sub>2</sub>. *ACS Nano* **5**, 9703–9709 (2011).
- Rodin, A. S., Carvalho, A. & Neto, A. C. Strain-induced gap modification in black phosphorus. *Phys. Rev. Lett.* **112**, 176801 (2014).
- Quereda, J. et al. Strong modulation of optical properties in black phosphorus through strain-engineered rippling. *Nano Lett.* **16**, 2931–2937 (2016).
- Zhang, Z. et al. Strain-modulated bandgap and piezo-resistive effect in black phosphorus field-effect transistors. *Nano Lett.* **17**, 6097–6103 (2017).
- Zhang, G. et al. Infrared fingerprints of few-layer black phosphorus. *Nat. Commun.* **8**, 14071 (2017).
- Çakir, D., Sahin, H. & Peeters, F. M. Tuning of the electronic and optical properties of single-layer black phosphorus by strain. *Phys. Rev. B Condens. Matter Mater. Phys.* **90**, 205421 (2014).
- Huang, S. et al. Strain-tunable van der Waals interactions in few-layer black phosphorus. *Nat. Commun.* **10**, 2447 (2019).
- Ma, W. et al. Piezoelectricity in multilayer black phosphorus for piezotronics and nanogenerators. *Adv. Mater.* **32**, 1905795 (2020).
- Sanchez-Perez, J. R. et al. Direct-bandgap light-emitting germanium in tensilely strained nanomembranes. *Proc. Natl Acad. Sci. USA* **108**, 18893–18898 (2011).
- Takei, K. et al. Quantum confinement effects in nanoscale-thickness InAs membranes. *Nano Lett.* **11**, 5008–5012 (2011).
- Ling, X., Wang, H., Huang, S., Xia, F. & Dresselhaus, M. S. The renaissance of black phosphorus. *Proc. Natl Acad. Sci. USA* **112**, 4523–4530 (2015).
- Ge, S. et al. Dynamical evolution of anisotropic response in black phosphorus under ultrafast photoexcitation. *Nano Lett.* **15**, 4650–4656 (2015).
- Bhaskar, P., Achtstein, A. W., Vermeulen, M. J. W. & Siebbeles, L. D. A. Radiatively dominated charge carrier recombination in black phosphorus. *J. Phys. Chem. C* **120**, 13836–13842 (2016).
- Chen, C. et al. Bright mid-infrared photoluminescence from thin-film black phosphorus. *Nano Lett.* **19**, 1488–1493 (2019).
- Du, Y. et al. Auxetic black phosphorus: a 2D material with negative Poisson's ratio. *Nano Lett.* **16**, 6701–6708 (2016).
- Wang, J. et al. Mid-infrared polarized emission from black phosphorus light-emitting diodes. *Nano Lett.* **20**, 3651–3655 (2020).
- Zong, X. et al. Black phosphorus-based van der Waals heterostructures for mid-infrared light-emission applications. *Light Sci. Appl.* **9**, 114 (2020).
- Chang, T.-Y. et al. Black phosphorus mid-infrared light-emitting diodes integrated with silicon photonic waveguides. *Nano Lett.* **20**, 6824–6830 (2020).
- Haug, A. Auger recombination in direct-gap semiconductors: band-structure effects. *J. Phys. C* **16**, 4159 (1983).
- Kurtz, S. R., Biefeld, R. M. & Dawson, L. R. Modification of valence-band symmetry and Auger threshold energy in biaxially compressed InAs<sub>x</sub>Sb<sub>y</sub>. *Phys. Rev. B* **51**, 7310 (1995).
- Lee, D.-D. & Lee, D.-S. Environmental gas sensors. *IEEE Sens. J.* **1**, 214–224 (2001).
- Dinh, T.-V., Choi, I.-Y., Son, Y.-S. & Kim, J.-C. A review on non-dispersive infrared gas sensors: improvement of sensor detection limit and interference correction. *Sens. Actuators B* **231**, 529–538 (2016).
- Gomes, J., Rodrigues, J. J., Rabélo, R. A., Kumar, N. & Kozlov, S. IoT-enabled gas sensors: technologies, applications, and opportunities. *J. Sens. Actuator Netw.* **8**, 57 (2019).
- Deng, Y. et al. Black phosphorus-monolayer MoS<sub>2</sub> van der Waals heterojunction p-n diode. *ACS Nano* **8**, 8292–8299 (2014).
- Youngblood, N., Chen, C., Koester, S. J. & Li, M. Waveguide-integrated black phosphorus photodetector with high responsivity and low dark current. *Nat. Photonics* **9**, 247–252 (2015).
- Yuan, H. et al. Polarization-sensitive broadband photodetector using a black phosphorus vertical p-n junction. *Nat. Nanotechnol.* **10**, 707–713 (2015).
- Guo, Q. et al. Black phosphorus mid-infrared photodetectors with high gain. *Nano Lett.* **16**, 4648–4655 (2016).
- Huang, M. et al. Broadband black-phosphorus photodetectors with high responsivity. *Adv. Mater.* **28**, 3481–3485 (2016).
- Chen, X. et al. Widely tunable black phosphorus mid-infrared photodetector. *Nat. Commun.* **8**, 1672 (2017).
- Bullock, J. et al. Polarization-resolved black phosphorus/molybdenum disulfide mid-wave infrared photodiodes with high detectivity at room temperature. *Nat. Photonics* **12**, 601–607 (2018).
- Amani, M., Regan, E., Bullock, J., Ahn, G. H. & Javey, A. Mid-wave infrared photoconductors based on black phosphorus-arsenic alloys. *ACS Nano* **11**, 11724–11731 (2017).

**Publisher's note** Springer Nature remains neutral with regard to jurisdictional claims in published maps and institutional affiliations.

© The Author(s), under exclusive licence to Springer Nature Limited 2021

# Article

## Methods

### Sample preparation

Crystals of black phosphorus (Smart Elements) were mechanically exfoliated onto a polydimethylsiloxane (PDMS) substrate ( $1 \times 1 \text{ cm}^2$ ) with PVC tape (catalogue number SPV224, Nitto). Before transfer, the crystal orientation of bP was identified by polarization-resolved Raman spectroscopy as described<sup>49</sup>. The transfer process used here is similar to the dry-transfer process described previously<sup>50</sup>. It was carried out in a modified optical microscope setup (Labophot, Nikon), with the sample stage replaced by a hotplate. A PETG substrate (2.54 mm thick; area  $3 \times 3 \text{ cm}^2$ ) was placed on a hotplate at 95 °C. The exfoliated bP on the PDMS stamp was positioned upside down and aligned with the centre of the PETG substrate. The stamp was slowly brought into contact with the thermally expanded PETG and bP was transferred at 95 °C. The bP-transferred PETG substrate was immediately subjected to rapid thermal quenching, bringing it down to room temperature. Owing to the CTE mismatch and the rapid thermal quenching process, bP is subject to biaxial compressive strain. After transfer, the prepared bP sample with biaxial compressive strain was loaded into a two-point bending apparatus (Extended Data Fig. 1a) inside an optical cryostat (catalogue number ST-100, Janis). All processes were performed inside a N<sub>2</sub>-purged glovebox (catalogue number 830-ABC, Plas-Labs) or in environments with minimum moisture and light exposure, to avoid any oxidation of bP induced by the ambient atmosphere.

### Device fabrication

For LED fabrication, we used electronic-grade polyimide (0.5 mm thick; area  $1 \times 1 \text{ cm}^2$ ) as a substrate instead of PETG, because of its compatibility with electron-beam lithography processes. Exfoliation and transfer of bP and MoS<sub>2</sub>, followed the procedure described above. Black phosphorus (thickness roughly 15–22 nm) was first transferred onto the polyimide substrate at 180 °C, and then rapidly quenched to room temperature. MoS<sub>2</sub> (roughly 10–15 nm thick; SPI Supplies), exfoliated on a PDMS stamp, was then transferred onto the top of the bP at room temperature to form an electron contact with the bP. Source and drain electrodes were patterned by conventional electron-beam lithography using a poly(methyl methacrylate) (PMMA) C4 resist (baked at 130 °C) and thermal evaporation of 40 nm Ni.

For photoconductor fabrication, we used bright-field-mode photolithography, followed by subtractive wet chemical etching, where the opaque portion of the photomask is the desired electrode patterns. First, we evaporated 100 nm Au onto the bP-transferred PETG (prepared as above). Then, S1818 (Shipley Microposit) was coated onto bP-transferred PETG and the sample was baked at 80 °C for 3 min, which is below the glass transition temperature of PETG (90–95 °C). After g-line exposure using a bright-field photomask, followed by development (using MF-26A, Microchem), the exposed Au region was completely etched using a gold etchant (potassium iodide, Transene). Finally, the residual photoresist layer was removed by flood exposure followed by the development process.

### Optical characterization

All optical measurements were carried out using a customized cryostat (catalogue number ST-100, Janis) with a CaF<sub>2</sub> window, which was evacuated to a base pressure of less than 10<sup>-5</sup> torr. A two-point bending apparatus was installed with the electric actuator inside the cryostat, so that the amount of uniaxial tensile strain could be simultaneously controlled during the measurement. For photoluminescence and electroluminescence measurements, a 15× reflective objective was installed at the auxiliary entrance port of a Fourier transform infrared (FT-IR) spectrometer (iSSO, Thermo Fisher), collecting the sample signal and sending it to the spectrometer, which was equipped with a CaF<sub>2</sub> beam splitter and a liquid N<sub>2</sub>-cooled HgCdTe (MCT) detector. A laser diode (Thorlabs;  $\lambda = 638 \text{ nm}$ ) and a laser diode controller (LDC500, Thorlabs)

were used as the excitation source for the photoluminescence measurements. A mirror was installed at the obscured centre of the reflective objective to reflect the focused excitation beam onto the sample. The polarization of the excitation laser was aligned to be parallel to the armchair orientation of bP by rotating the polarization plane using a linear polarizer followed by a half-wave plate. For electroluminescence measurements, a voltage-controlled current source (catalogue number CS580, Stanford Research Systems) was used to apply a forward current bias. The instrument response function of the setup accounted for different wavelengths and polarizations, as described<sup>47</sup>. To calculate spectra, we used double modulation to separate the photoluminescence/electroluminescence signal from the thermal background in the modulated interferogram, which was obtained using a lock-in amplifier (SR865, Stanford Research Systems) and a low-noise voltage preamplifier (SR560, Stanford Research Systems). Details of the setup for measuring photoluminescence and electroluminescence are described further in Extended Data Fig. 8.

The bP photodetector was characterized at the auxiliary exit port of the FT-IR spectrometer, where the photoconductor was excited by modulated 1,000 K blackbody illumination. The device was biased at 100 mV. The generated photocurrent was amplified using a low-noise current preamplifier (SR570, Stanford Research Systems) and sent to the external detector interface of the FT-IR system, in order to resolve the full spectral responsivity. A BaF<sub>2</sub> linear polarizer was placed in the unpolarized excitation path for the polarization-resolved photoresponse measurements. For temporal photoresponse measurements, a laser diode (Thorlabs;  $\lambda = 1,650 \text{ nm}$ ) was modulated by a square wave generated using a function generator (81150A, Agilent). The FT-IR system was calibrated following as described<sup>47</sup>. An internal deuterated triglycine sulfate (DTGS) detector was used to measure the relative spectral intensity of the excitation. A Ge photodiode (Thorlabs; calibrated by the National Institute of Standards and Technology (NIST)) and InSb photodiode (Teledyne Judson Technologies) were used as reference to determine the absolute responsivity of our bP photoconductors, as a function of wavelength. Raman measurements were performed in a commercial setup (inVia, Renishaw) with 532-nm laser excitation, which was linearly polarized along 45° with respect to the armchair and zigzag orientations of bP, in order to optimize the signal intensity from all three characteristic Raman modes (A<sub>g</sub><sup>1</sup>, B<sub>2g</sub>, and A<sub>g</sub><sup>2</sup>) at the same time. For both photoluminescence and Raman measurements, we used the lowest excitation power that gave a perceptible signal-to-noise ratio (SNR), to prevent any localized heat-induced strain effects in bP. The effects of laser-induced heating on the strain conditions of bP are characterized in Extended Data Fig. 2b.

### Characterization of NDIR gas sensing

In the NDIR gas-sensing setup, target gases and diluent gas (N<sub>2</sub>) were injected into an enclosed gas cell, which was illuminated by the bP LED at one end. At the opposite end, a commercial InSb photodiode was used to measure the light intensity passing through the gas cell (Fig. 4a). Electroluminescence spectra (Fig. 4b, c) were measured by the internal MCT detector in the FT-IR system, under the constant flow of a target gas at various concentrations. Responses of the NDIR gas sensor (Fig. 4d, e and Extended Data Fig. 5b, c) were characterized by a commercial liquid N<sub>2</sub>-cooled InSb photodiode using a sequence of pulses of target gases and purging cycles of N<sub>2</sub> gas. A pair of CaF<sub>2</sub> plano-convex lenses or 15× reflective objectives was used to improve the dynamic range of the measurements. A motorized filter wheel (catalogue number FW102C, Thorlabs) was used with bandpass filters to detect H<sub>2</sub>O (centre wavelength (CWL) = 2,700 nm; Iridian), CH<sub>4</sub> (CWL = 3,330 nm; Thorlabs) and CO<sub>2</sub> (CWL = 4,260 nm; Thorlabs). The bP LED was modulated at 1 kHz, and the generated photocurrent for the InSb photodiode was amplified using a low-noise current preamplifier (Stanford Research Systems) and measured using a lock-in amplifier (Stanford Research Systems). Separate cylinders containing CH<sub>4</sub> gas (2.5%),

$\text{CO}_2$  gas (more than 99.9%), and moisture-containing  $\text{N}_2$  gas were connected to individual mass flow controllers (Alicat) to mix and deliver the gas pulse with precise concentrations. Humidity inside the gas cell was monitored using a commercial digital humidity sensor (SHT2x, Sensirion). At room temperature (292–295 K), the current density was kept at  $20 \text{ A cm}^{-2}$  for all measurements using a 20 nm bP LED. Note that the baseline current ( $I_{\text{N}_2}$ ) was different when the system was configured to sense the different gases. This is attributed to the changing emission intensity from the bP LED in response to applied strain conditions, the different transmission values of the filters used to detect each gas, and the varying spectral responses of the InSb photodiode.

### Black phosphorus for strain application

Exfoliated bP flakes with cracks or wrinkles did not show any strain-induced bandgap modification with our methods. We thus made substantial efforts during sample preparation and fabrication to avoid cracks or wrinkles within bP flakes. We focused mainly on demonstrating bandgap tuning and its device applications for bP with thicknesses of 15–22 nm. For this thickness range, carrier transport is less susceptible to the environment than in thinner bP, while strain-induced bandgap tuning has a higher yield than its thicker counterpart. We found that the strain-induced bandgap modification using our method started to become less effective for bP thicker than 22 nm, possibly because of slippage between bP and substrate. On the other hand, bP thinner than 15 nm had a lower yield of bandgap tuning by strain, which could be attributed to the difficulty in processing thinner bP without cracks, and accelerated oxidation in thinner bP from layer-by-layer thinning<sup>51</sup>. As it is challenging to use direct atomic force microscopy (AFM) to characterize the thickness of bP on a soft polymer substrate, we used the method described previously<sup>20</sup> to identify bP with a suitable thickness.

### Compressive strain application

To apply compressive strain, we first attempted to use negative bending (that is, bending in the opposite direction to that used for tensile strain). However, this induced decoupling of bP from the substrate and buckling of bP, possibly because of the Poisson effect. Therefore, to apply compressive strain, we instead used the thermal expansion mismatch between bP and substrate. We selected PETG for the substrate because we found it to have favourable properties compared with other polymers (for example, polypropylene, polyethylene, ethylene-vinyl acetate (EVA), polycarbonate, polyvinylidene fluoride (PVDF), PDMS, nylon, polyvinyl chloride (PVC), polystyrene and Teflon). We used a transfer temperature of 95 °C, which is close to the glass transition temperature of PETG. We experimentally measured the CTE of PETG to be  $80.5 \pm 2.5 \text{ ppm } ^\circ\text{C}^{-1}$  and  $520 \pm 32 \text{ ppm } ^\circ\text{C}^{-1}$  over temperature ranges of 20–90 °C and 90–95 °C, respectively, indicating that the thermal expansion rate rapidly increases at the glass transition temperature<sup>52</sup>. We also found that the higher transfer temperature ( $T=100$  °C) resulted in wrinkles and delamination of bP owing to the low adhesion and excessive compressive strain from the substrate<sup>53</sup> and did not contribute to a larger modulation range by strain. Therefore, we did not use transfer temperatures in excess of 95 °C. Black phosphorus has anisotropic CTEs of 33 (armchair) and 22 (zigzag)  $\text{ppm } ^\circ\text{C}^{-1}$  (ref. <sup>54</sup>). The compressive strain applied in bP due to the CTE mismatch can thus be calculated as follows:

$$\varepsilon(T_{\text{tr}}) = \int_{20^\circ\text{C}}^{T_{\text{tr}}} \alpha_{\text{sub}}(T) dT - \int_{20^\circ\text{C}}^{T_{\text{tr}}} \alpha_{\text{bp}}(T) dT$$

where  $T_{\text{tr}}$  is the transfer temperature of bP onto the substrate;  $\alpha_{\text{sub}}$  is the CTE of the substrate; and  $\alpha_{\text{bp}}$  is the CTE of bP. The compressive strain resulting from this quenching process was 0.58% in the armchair direction and 0.66% in the zigzag direction. The strain in the armchair ( $x$ ) direction can be obtained using the Poisson's ratio of bP.

### Substrate for device fabrication

The chemical instability of bP has been a major roadblock in demonstrating strain-tunable optoelectronic devices based on bP. Here we have developed a method and procedure that are compatible with conventional lithography, while maintaining the material composition and device performance of bP. Although the polyimide has a lower CTE (experimentally measured to be  $34.8 \pm 1.5 \text{ ppm } ^\circ\text{C}^{-1}$  at 20–200 °C) and is less soft than PETG, we used it for bP–MoS<sub>2</sub> LEDs for following reasons. Polyimide is chemically stable, resistant to high temperatures (greater than 100 °C), and compatible with conventional lithography processes and organic solvent processing. These enable electrode patterning with a desired shape and higher spatial resolution, reducing the series resistance of the LEDs. In addition, the electronic-grade polyimide we use has a higher thermal conductivity than PETG, which is advantageous for repeated operations over long periods of time without performance degradation due to thermal failure and charging issues. Note that compressive strain in bP–MoS<sub>2</sub> LEDs is not completely released during the high-temperature measurement (Extended Data Fig. 4) because of the low CTE of the polyimide substrate.

### Preserving strain and stability during fabrication

The built-in strain between a 2D transition-metal dichalcogenide (TMDC) monolayer and the substrate can be released by solvent-evaporation-mediated decoupling<sup>55</sup>. However, we find that our bP–MoS<sub>2</sub> LED still preserved partial compressive strain after fabrication. This can be attributed to the source/drain electrodes and to MoS<sub>2</sub> being on top of the bP, both of which serve as a clamp to prevent the complete release of the biaxial compressive strain between bP and the polyimide substrate. During the lift-off process acetone evaporation was avoided, and toluene was used instead of isopropyl alcohol (IPA), preventing the release the built-in strain in 2D materials due to evaporation. For the fabrication of the bP photoconductor, the photoresist developer (MF-26A) and the gold etchant (potassium iodide) did not affect the biaxial compressive strain in bP, which was mostly maintained after the fabrication was completed. Moreover, the gold film evaporated on bP could have functioned as a clamping agent, adding/holding the biaxial compressive strain in bP. We reported previously that metal evaporation on 2D materials results in biaxial compressive strain owing to the thermal expansion mismatch between the metal and material<sup>56,57</sup>. During photoconductor fabrication, except during the 5 s of g-line exposure, we minimized the exposure of bP to visible light in order to prevent photooxidation. In agreement with previous work<sup>58</sup>, we observed that the gold etchant (potassium iodide) and deionized water alone did not induce bP oxidation and that the device performance was not degraded during fabrication. It is understood that water, oxygen and visible light are simultaneously required for oxidation of bP.

### Measurement accuracy

Rather than using extinction spectra to estimate the bandgap, we instead used IRPL spectroscopy to characterize the bandgap modification in bP under strain. For measurement of electroluminescence and photoluminescence, we note that the measurement setup was calibrated for each value of strain, in order to capture the absolute intensity of light emission from the non-planar surface. This was required in order to exclude the possibility of drift of the focal plane upon bending of the substrate. For the photoluminescence measurements, the spot size of the excitation laser (roughly  $1,600 \mu\text{m}^2$ ) was kept slightly smaller than the size of the bP flake. At each measurement, the polarization of excitation with respect to the crystal orientation of the bP was verified by comparing the results obtained when rotating the polarizer in the excitation path versus rotating the sample with respect to a fixed laser polarization. We found that absorption by bP at the photoluminescence excitation wavelength (638 nm) was weakly dependent on the polarization angle, although it is expected to have the highest anisotropy near

# Article

the absorption edge<sup>43</sup>. For photoconductor characterization, we used a fixed voltage bias of  $V_{ds} = 100$  mV (smaller than the bP bandgap) for all measurements in order to maintain the responsivity of the photoconductor in a linear regime.

## Calibration of LED efficiency

To quantify the light-emission efficiency of our bP LEDs, we used a 4.05-μm quantum cascade laser (QF4050T1, Thorlabs) and an infrared reflectance standard (Labsphere). We measured the laser output power using a high-sensitivity thermal power sensor (Ophir) at the focal plane of the objective. We measured the laser signal intensity reflected by the Lambertian reflectance standard at the focal plane by using the FT-IR spectrometer under the same measurement conditions. Using the ratio of the output power measured from the power sensor to the signal intensity measured by the MCT detector in the FT-IR spectrometer, we can convert the emission intensity from bP LED measured by the FT-IR spectrometer into output power. The instrument response function (IRF) of the MCT detector is taken into consideration when accounting for the difference between the laser and bP LED emission wavelengths. In addition, as the reflective objective has a fixed collection angle, we calculated the angular collection factor in order to account for the difference between the angular distribution of emission of the bPLEDs and of the Lambertian emitter. The output power of our bP LED is then calculated by:

$$\text{Power}_{\text{bPLED}} = \text{Intensity}_{\text{bPLED(FTIR)}} \times \frac{\text{Power}_{\text{laser(power meter)}}}{\text{Intensity}_{\text{laser(FTIR)}}} \\ \times \frac{\text{IRF}(\lambda_{\text{bPLED}})}{\text{IRF}(\lambda = 4.05 \mu\text{m})} \times \frac{\text{Angular collection}_{\text{bPLED}}}{\text{Angular collection}_{\text{laser}}}$$

where  $\text{IRF}(\lambda_{\text{bPLED}})$  and  $\text{IRF}(\lambda = 4.05 \mu\text{m})$  are the instrument response function of the MCT detector at the bP LED emission wavelength and at 4.05 μm, respectively; and  $\text{Angular collection}_{\text{bPLED}}$  and  $\text{Angular collection}_{\text{laser}}$  are the collected signal with the objective lens when the on-axis ( $0^\circ$ ) emission intensity is assumed to be 1. Note that in order to estimate the instantaneous carrier concentration in the bP LED at different current densities in Fig. 3f, we assume that the carriers are uniformly distributed in the bP volume.

## Strain-tunable photodetection

As expected from the highly polarization-dependent absorption of bP<sup>59</sup>, we observed the highest photoresponse when light was polarized in the armchair direction, and the lowest photoresponse when it was polarized in the zigzag direction (Extended Data Fig. 6e). The  $I$ - $V$ -characteristics of the photoconductors under compressive and tensile strain showed no obvious difference (Extended Data Fig. 6f). Under compressive strain, the rise and fall times of the photoconductors were 18.6 μs and 16.3 μs, respectively (Extended Data Fig. 6g). Under tensile strain, they showed similar values of 18.7 μs and 16.6 μs, respectively. The noise current density did not show any substantial variation between compressive strain and tensile strain, and the low frequency noise was dominated by the contribution from  $1/f$  noise (Extended Data Fig. 7a).

To estimate the performance of our tunable photoconductor, we calculated the specific detectivity ( $D^*$ ) as  $D^* = \sqrt{A\Delta f}/\text{NEP}$ , where  $A$  is the device area,  $\Delta f$  is the bandwidth, and NEP is the noise equivalent power. We measured the bandwidth of the photoconductor to be 10 kHz under both compressive and tensile strain (Extended Data Fig. 7b). A detailed discussion of the process we used to estimate NEP is provided below (where we use the experimentally extracted noise current to avoid an overestimation of  $D^*$ ). Given a constant device area and integration time, the optimum bP thickness that maximizes the  $D^*$  of a bP photoconductor is reported to be roughly 25–35 nm, which originates from the balance between increasing absorption from greater thickness and reducing noise in fewer layers<sup>48</sup>. By applying

strain to a photoconductor based on bP with a thickness close to this range, we can extend its spectral photoresponse while preserving optimal device performance. The detectivity could be further improved by enhancing the light-collection efficiency of the device and/or implementing a gate bias to compensate for background doping<sup>47,48</sup>.

## Calculation of NEP

NEP is the optical power that gives a SNR of unity for a given measurement bandwidth of a photodetector. It is determined by calculating the photocurrent ( $I_{\text{ph}} = \text{responsivity} (R_A) \times \text{NEP}$ ) when  $\text{SNR} = 1 = I_{\text{ph}}^2/\langle i_n^2 \rangle$ . As the total noise current is determined mainly by the sum of the contributions from shot noise and Johnson noise, we can formulate it as follows:  $\langle i_n^2 \rangle = 2e(I_{\text{ph}} + I_{\text{dark}})\Delta f + \frac{4k_B T}{R}\Delta f$ , where  $e$  is the electron charge, and  $R$  is the dark resistance which is determined from the  $I$ - $V$  characteristics of the photoconductor (Extended Data Fig. 6f). Solving the equation ( $I_{\text{ph}}^2 - 2e(I_{\text{ph}} + I_{\text{dark}})\Delta f + \frac{4k_B T}{R}\Delta f = 0$ ) gives the value of  $I_{\text{ph}}$ , with all the other parameters in the equation obtained from the experimental data. Therefore, NEP is calculated as  $6.54476 \times 10^{-11}/R_A^{\text{compressive}}$  for compressive strain and  $6.69445 \times 10^{-11}/R_A^{\text{tensile}}$  for tensile strain.

## Data availability

All data generated or analysed during this study are included in this published article. Source data are provided with this paper.

49. Wu, J., Mao, N., Xie, L., Xu, H. & Zhang, J. Identifying the crystalline orientation of black phosphorus using angle-resolved polarized Raman spectroscopy. *Angew. Chem. Int. Ed.* **54**, 2366–2369 (2015).
50. Castellanos-Gomez, A. et al. Deterministic transfer of two-dimensional materials by all-dry viscoelastic stamping. *2D Mater.* **1**, 011002 (2014).
51. Favron, A. et al. Photooxidation and quantum confinement effects in exfoliated black phosphorus. *Nat. Mater.* **14**, 826–832 (2015).
52. Foo, E., Jaafar, M., Aziz, A. & Sim, L. C. Properties of spin coated epoxy/silica thin film composites: effect of nano- and micron-size fillers. *Compos. Part A Appl. Sci. Manuf.* **42**, 1432–1437 (2011).
53. Mei, H., Landis, C. M. & Huang, R. Concomitant wrinkling and buckle-delamination of elastic thin films on compliant substrates. *Mech. Mater.* **43**, 627–642 (2011).
54. Madelung, O. *Semiconductors: Data Handbook* (3rd edn) (Springer, Berlin, 2004).
55. Kim, H. et al. Synthetic WSe<sub>2</sub> monolayers with high photoluminescence quantum yield. *Sci. Adv.* **5**, eaau4728 (2019).
56. Gramling, H. M. et al. Spatially precise transfer of patterned monolayer WS<sub>2</sub> and MoS<sub>2</sub> with features larger than 10<sup>4</sup> μm<sup>2</sup> directly from multilayer sources. *ACS Appl. Electron. Mater.* **1**, 407–416 (2019).
57. Nguyen, V. et al. Deterministic assembly of arrays of lithographically defined WS<sub>2</sub> and MoS<sub>2</sub> monolayer features directly from multilayer sources into van der Waals heterostructures. *J. Micro Nano-Manuf.* **7**, 041006 (2019).
58. Huang, Y. et al. Interaction of black phosphorus with oxygen and water. *Chem. Mater.* **28**, 8330–8339 (2016).
59. Qiao, J., Kong, X., Hu, Z. X., Yang, F. & Ji, W. High-mobility transport anisotropy and linear dichroism in few-layer black phosphorus. *Nat. Commun.* **5**, 4475 (2014).
60. Desai, S. B. et al. Strain-induced indirect to direct bandgap transition in multilayer WSe<sub>2</sub>. *Nano Lett.* **14**, 4592–4597 (2014).
61. Matthewson, M. J., Kurkjian, C. R. & Gulati, S. T. Strength measurement of optical fibers by bending. *J. Am. Ceram. Soc.* **69**, 815–821 (1986).
62. Plechinger, G. et al. Control of biaxial strain in single-layer molybdenite using local thermal expansion of the substrate. *2D Mater.* **2**, 015006 (2015).
63. Luo, W., Song, Q., Zhou, G., Tuschel, D. & Xia, G. Study of black phosphorus using angle-resolved polarized Raman spectroscopy with 442 nm excitation. Preprint at <https://arxiv.org/abs/1610.03382> (2016).
64. Zhang, Z. M., Lefever-Button, G. & Powell, F. R. Infrared refractive index and extinction coefficient of polyimide films. *Int. J. Thermophys.* **19**, 905–916 (1998).
65. Sherrrott, M. C. et al. Anisotropic quantum well electro-optics in few-layer black phosphorus. *Nano Lett.* **19**, 269–276 (2019).
66. Beal, A. R. & Hughes, H. P. Kramers-Kronig analysis of the reflectivity spectra of 2H-MoS<sub>2</sub>, 2H-MoSe<sub>2</sub> and 2H-MoTe<sub>2</sub>. *J. Phys. Chem.* **12**, 881 (1979).
67. Hori, Y., Ando, Y., Miyamoto, Y. & Sugino, O. Effect of strain on band structure and electron transport in InAs. *Solid-State Electron.* **43**, 1813–1816 (1999).
68. Delimitis, A. et al. Strain distribution of thin InN epilayers grown on (0001) GaN templates by molecular beam epitaxy. *Appl. Phys. Lett.* **90**, 061920 (2007).
69. Orsal, G. et al. Bandgap energy bowing parameter of strained and relaxed InGaN layers. *Opt. Mater. Express* **4**, 1030–1041 (2014).
70. Varshni, Y. P. Band-to-band radiative recombination in groups IV, VI, and III-V semiconductors (I). *Phys. Status Solidi* **19**, 459 (1967).
71. Vodopyanov, K. L., Graener, H., Phillips, C. C. & Tate, T. J. Picosecond carrier dynamics and studies of Auger recombination processes in indium arsenide at room temperature. *Phys. Rev. B* **46**, 13194 (1992).
72. Rogalski, A. & Józwikowski, K. The intrinsic carrier concentration in Pb<sub>1-x</sub>Sn<sub>x</sub>Te, Pb<sub>1-x</sub>Sn<sub>x</sub>Se, and PbS<sub>1-x</sub>Se<sub>x</sub>. *Phys. Status Solidi* **111**, 559 (1989).

73. Klann, R., Höfer, T. & Buhleier, R. Fast recombination processes in lead chalcogenide semiconductors studied via transient optical nonlinearities. *J. Appl. Phys.* **77**, 277 (1995).
74. Marchetti, S., Martinelli, M. & Simili, R. The Auger recombination coefficient in InAs and GaSb derived from the infrared dynamical plasma reflectivity. *J. Phys. Condens. Matter* **14**, 3653–3656 (2002).

**Acknowledgements** We thank H. M. Fahad for help with setting up the gas-sensing instrument. Luminescence studies were funded by the US Department of Energy, Office of Science, Office of Basic Energy Sciences, Materials Sciences and Engineering Division under contract DE-AC02-05-CH11231 (EMAT program KC1201). Photodetector fabrication and testing were funded by the Defense Advanced Research Projects Agency under contract HR0011-16-1-0004. K.B.C. acknowledges funding from the Australian Research Council (grant numbers DP180104141 and FT140100577). H.K. acknowledges support from Samsung Scholarship.

**Author contributions** H.K. and A.J. conceived the idea for the project and designed the experiments. H.K., S.Z.U. and D.-H.L. performed optical measurements. H.K., M.Y. and T.K. fabricated devices. S.Z.U., N.S.A., S.B. and K.B.C. performed optical simulations. N.G. helped with gas-sensing experiments. Y.R. and C.P.G. helped with Raman measurements. H.K. wrote the manuscript. All authors discussed the results and commented on the manuscript.

**Competing interests** The authors declare no competing interests.

**Additional information**

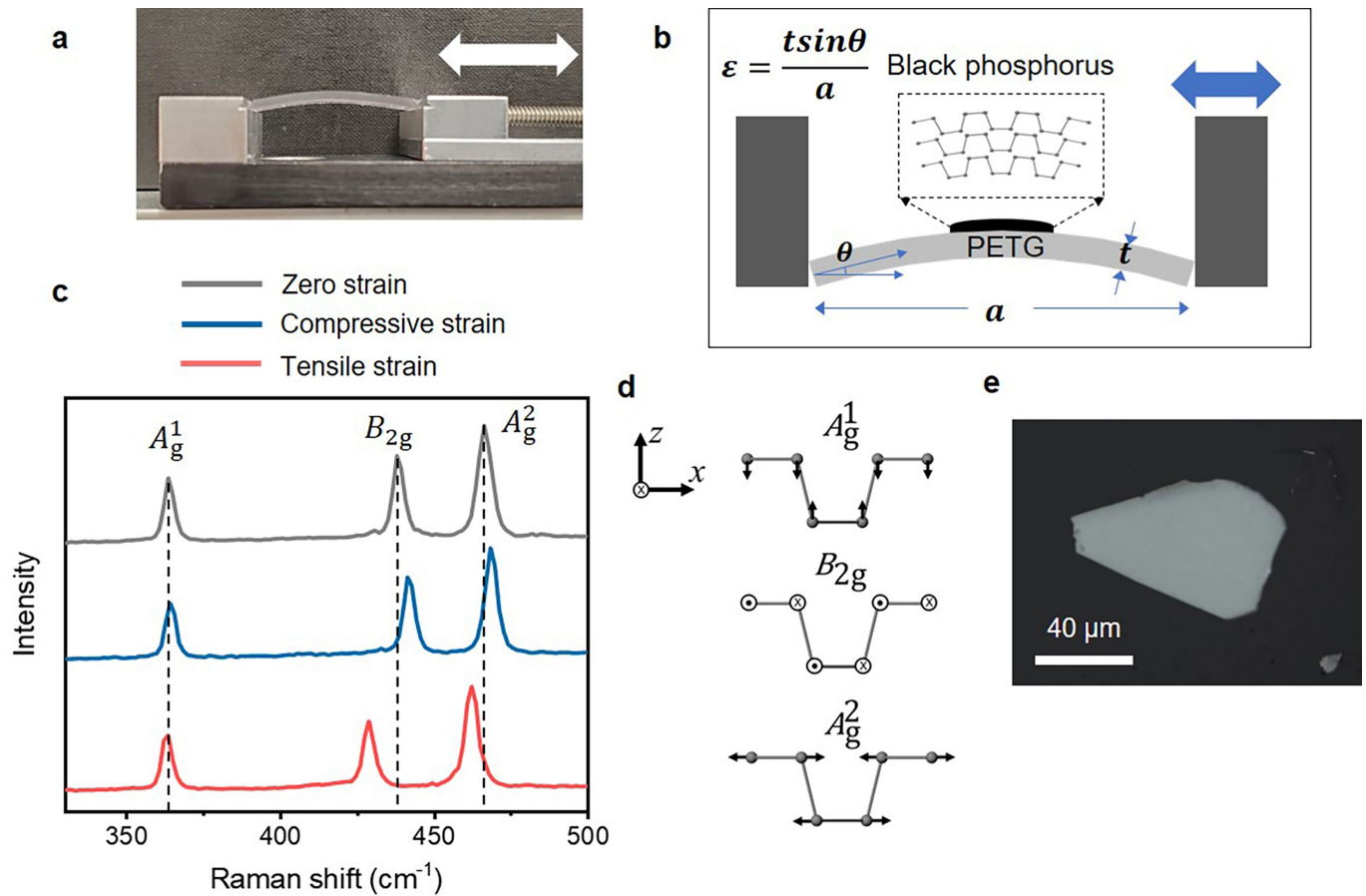
**Supplementary information** The online version contains supplementary material available at <https://doi.org/10.1038/s41586-021-03701-1>.

**Correspondence and requests for materials** should be addressed to A.J.

**Peer review information** *Nature* thanks Kah Wee Ang, Andres Castellanos-Gomez and the other, anonymous, reviewer(s) for their contribution to the peer review of this work.

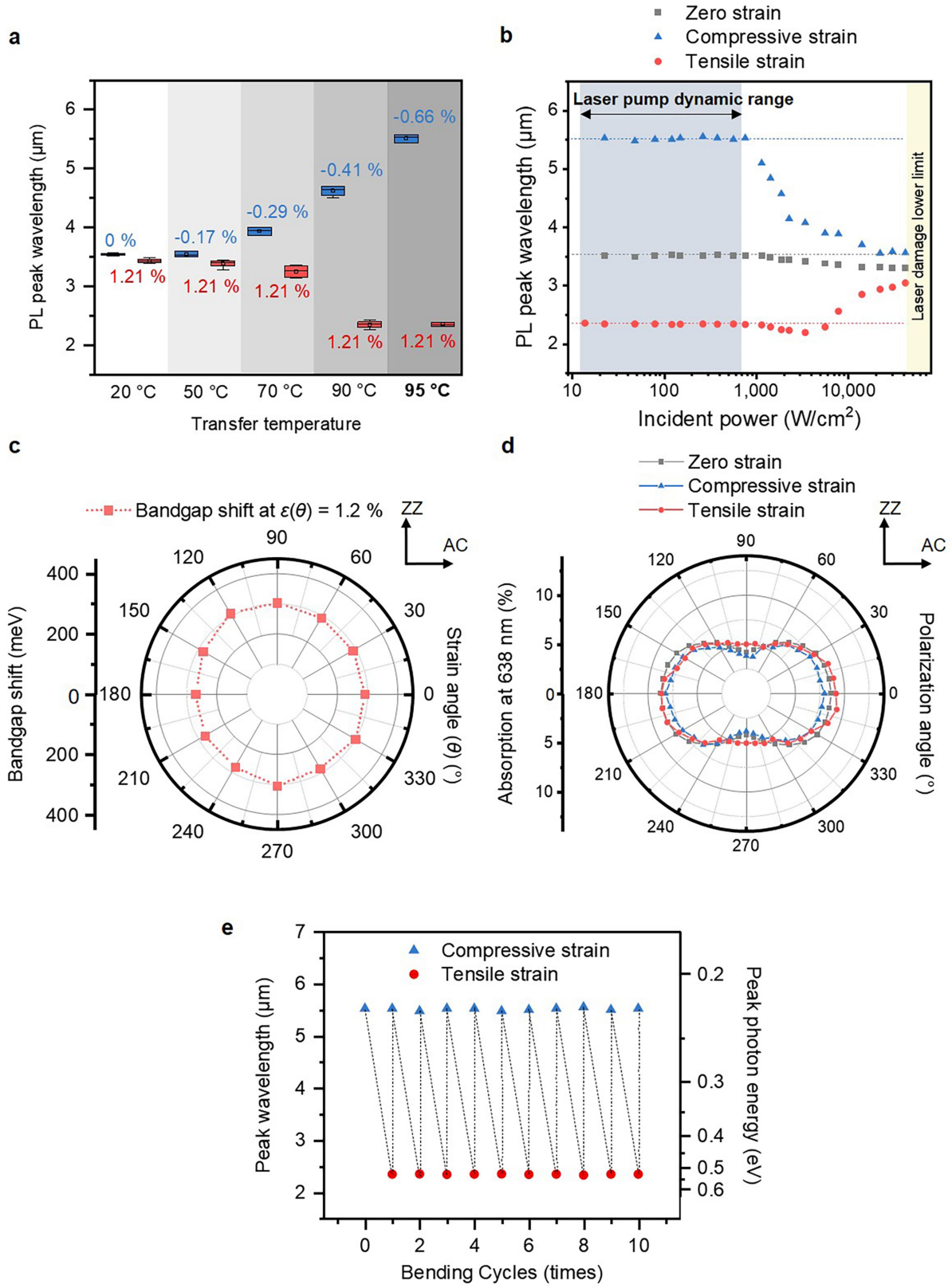
**Reprints and permissions information** is available at <http://www.nature.com/reprints>.

# Article



**Extended Data Fig. 1 | Strain applied in bP.** **a**, Photographic image of the two-point bending apparatus used here. An electrical linear actuator that can push/pull one point of the two-point bending apparatus applies a continuous and precise amount of uniaxial tensile strain to bP. **b**, Schematic of the two-point bending apparatus. Strain is calculated as  $\varepsilon = ts\sin\theta/a$ , where  $\varepsilon$  is the amount of strain;  $t$  is the thickness of the substrate;  $a$  is the length of the substrate; and  $\theta$  represents the angle of bending, which is equal to  $a/(2R)$  where

$R$  is the radius of the curvature<sup>60</sup>. Note that the circular arc approximation is not satisfied when  $\theta$  is large at strains of 20% or more<sup>61</sup>. **c**, Raman spectra of the bP measured in Fig. 1 and Fig. 2. **d**, Schematic showing the atomic vibrations that correspond to Raman modes of  $A_g^1$  (out-of-plane),  $B_{2g}$  (in-plane; zigzag), and  $A_g^2$  (in-plane; armchair). **e**, Optical image of the strained bP flake on the PETG substrate.



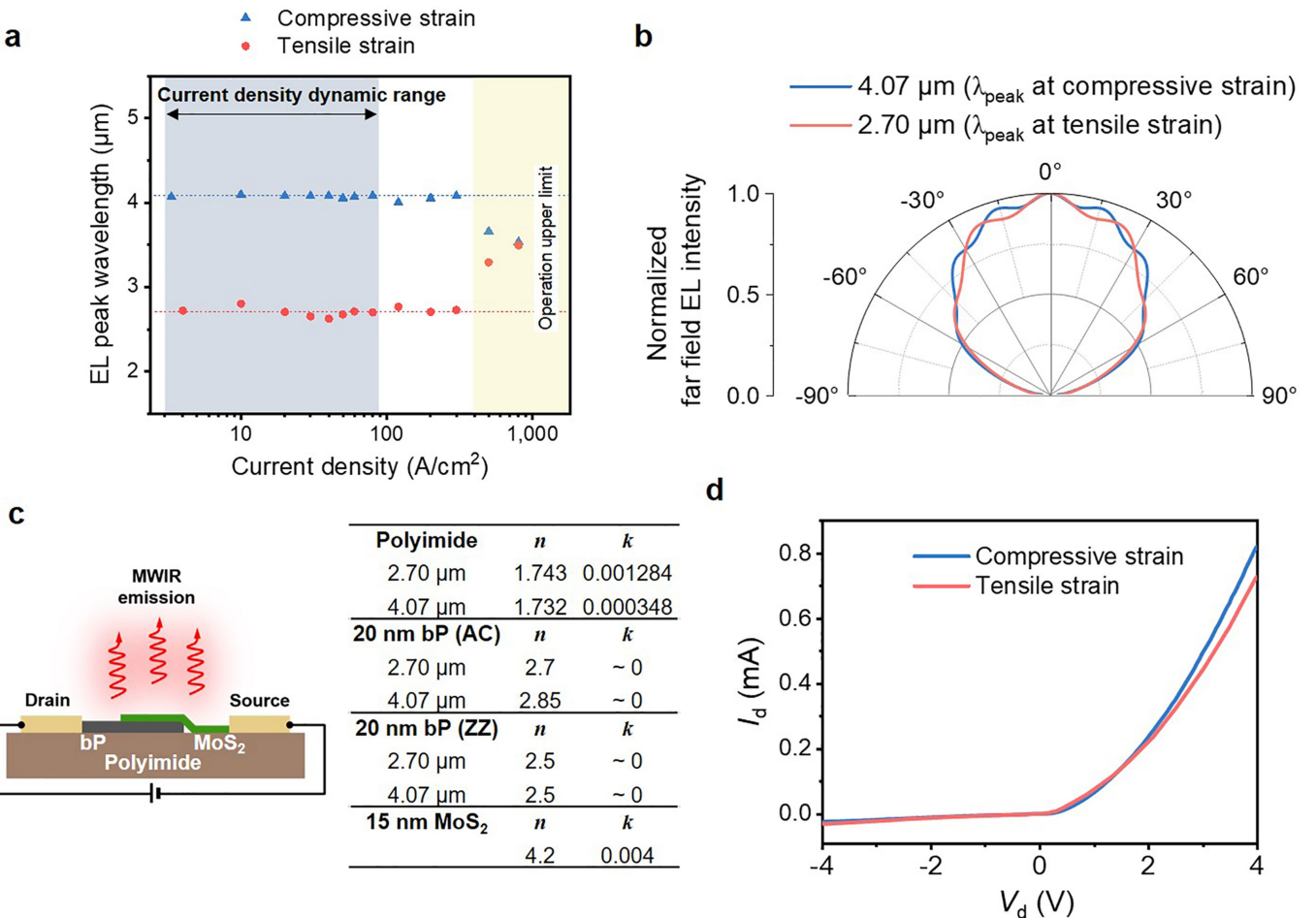
**Extended Data Fig. 2** | See next page for caption.

# Article

## Extended Data Fig. 2 | Detailed optical characterization of strained bP.

**a**, Photoluminescence (PL) peak wavelength as a function of transfer temperature. We characterized the photoluminescence peak wavelength as a function of biaxial compressive strain before and after the application of tensile strain (1.21%, zigzag). Each measurement was performed for five bP samples with thickness 20–22 nm. Samples were compressively strained by different amounts via different transfer temperatures ( $T_{tr} = 20\text{ }^{\circ}\text{C}$ , 50  $^{\circ}\text{C}$ , 70  $^{\circ}\text{C}$ , 90  $^{\circ}\text{C}$  and 95  $^{\circ}\text{C}$ ). The photoluminescence peak shift resulting from tensile strain increased with increasing biaxial compressive strain (as determined by transfer temperature). This is understood to be the result of the following. At high biaxial strain, the larger friction-induced resistance prevents the sliding of the 2D materials<sup>55</sup>. At lower transfer temperatures—that is, with reduced biaxial compressive strain—the bP is thus more likely to slip during bending of the substrate, such that the intended uniaxial tensile strain is not efficiently delivered to the bP. This could be because, at lower values of biaxial strain (that is, lower transfer temperatures), the friction-induced resistance that would prevent sliding of the bP is reduced. **b**, Laser power dependence of strain effect. We characterized the laser-induced heating effect on the bandgap shift by measuring photoluminescence peak wavelengths as a function of laser power. As the excitation spot size was similar or slightly smaller than the bP size, this helped to prevent the thermal expansion of the surrounding PETG by laser excitation (this thermal expansion could have elicited unexpected strain or slippage of bP from the PETG<sup>62</sup>). Regardless of the strain in bP, an excitation power higher than 1,500 W cm<sup>-2</sup> always resulted in blueshift of the photoluminescence, attributed to thermal heating by the laser<sup>63</sup>. Although the

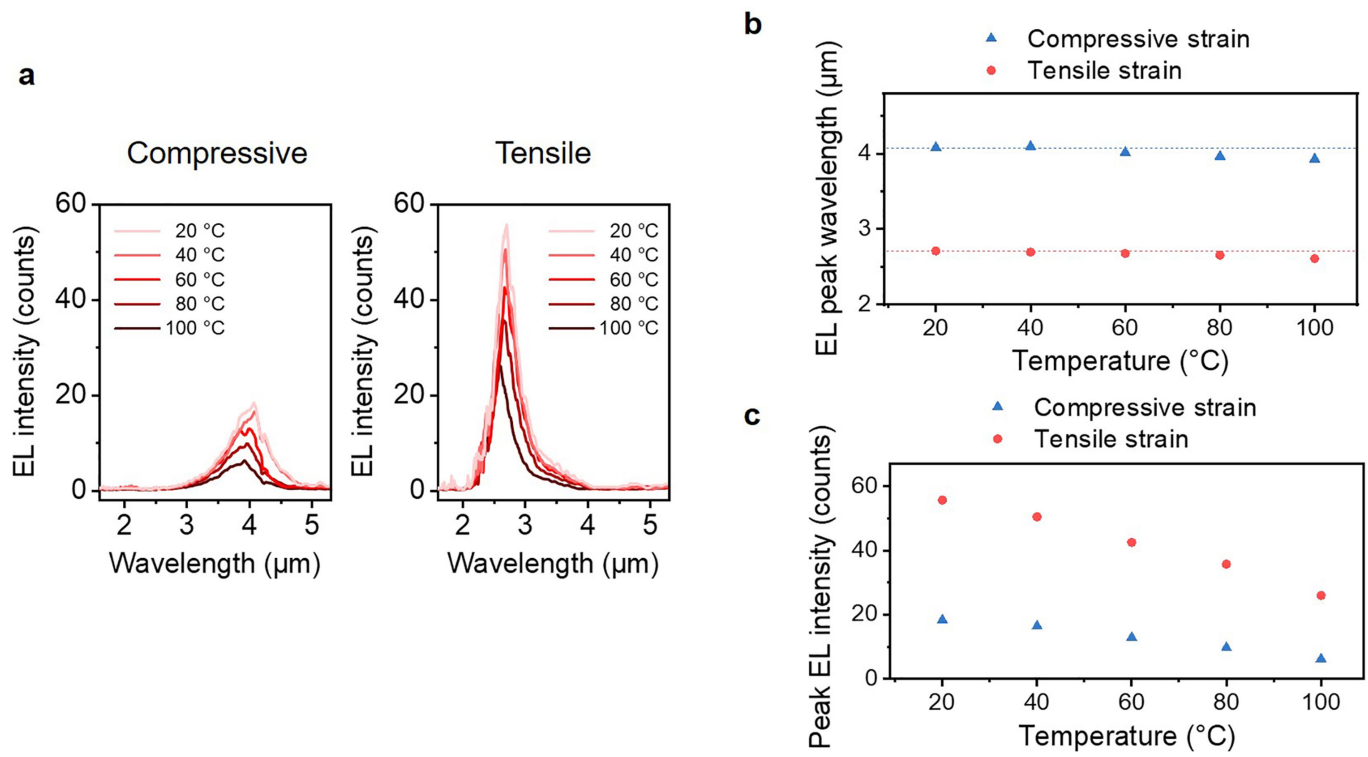
photoluminescence peak position recovered after cooling to room temperature without excitation, when the laser intensity was even higher (higher than around 20 kW cm<sup>-2</sup>), there was visible damage to bP, which did not return to its original photoluminescence peak position. Therefore, we kept the laser incident power for photoluminescence measurements below 600 W cm<sup>-2</sup>, such that the photoluminescence peak of the exfoliated sample remained constant. This laser incident power is much less than that of the least powerful laser pump (roughly 20 kW cm<sup>-2</sup>), a value that is known to have a laser thermal effect in bP and MoS<sub>2</sub> transferred on polyimide or PDMS<sup>62,63</sup>. **c**, Bandgap shift under different directions of strain with respect to the crystal orientation of bP. As the direction of tensile strain changed with respect to the crystal orientation of bP, there was no apparent difference in the strain-induced bandgap shift. This observation is consistent with previous results from a similar bending experiment performed on six-layer bP atop a polyethylene terephthalate (PET) substrate<sup>22</sup>. AC, armchair; ZZ, zigzag. **d**, Absorption at excitation wavelength for bP under zero strain, compressive strain and 1.21% of tensile strain. We found that strain had no notable effects on the absorption of light by bP at the photoluminescence excitation wavelength. Even though the bP bandgap was being modulated by strain, because our excitation wavelength was far from the absorption edge, the enhancement in photoluminescence cannot be attributed to increased absorption. **e**, Reversibility and repeatability of bandgap tuning in bP using compressive strain (0.6%) and tensile strain (1.2%). The photoluminescence peak from 20 nm bP shifts and recovers throughout ten cycles of bending and relaxation. At much higher strain, the PETG is subject to plastic deformation, exhibiting no return to its original state.



**Extended Data Fig. 3 | Detailed characterization of variable-spectrum bP**

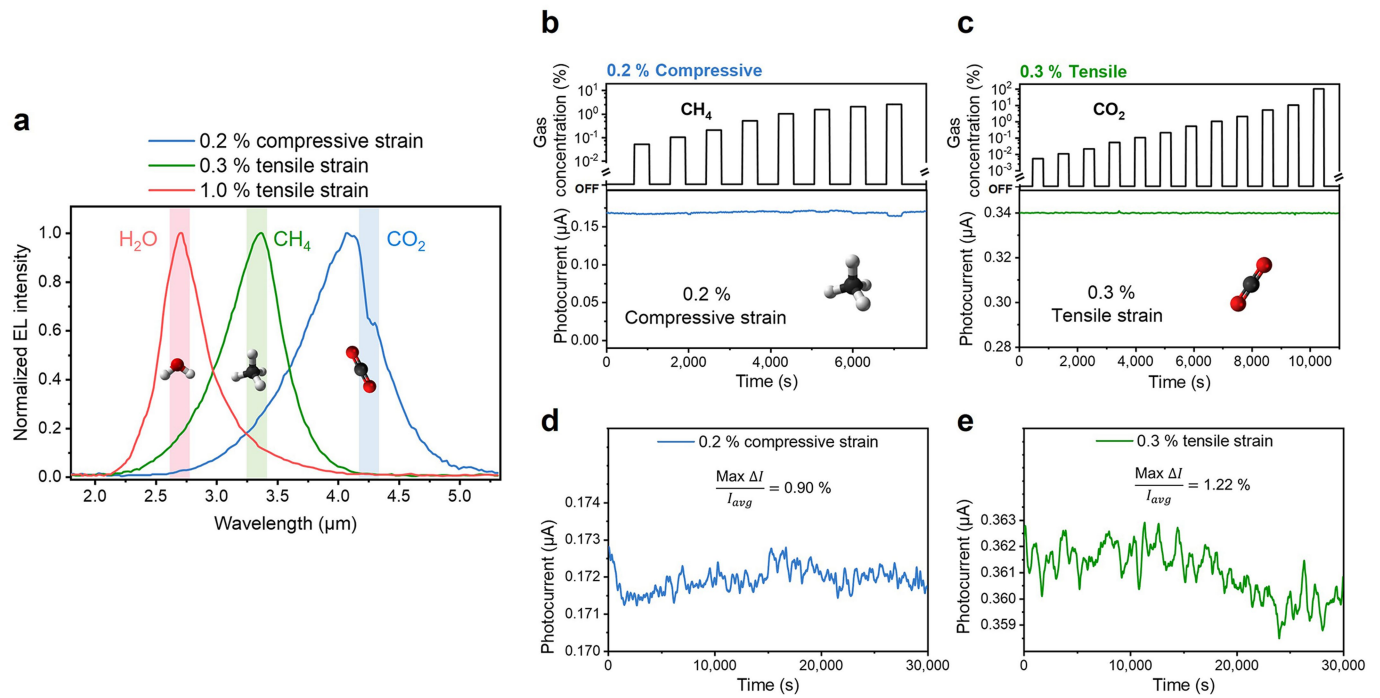
**LED.** **a**, Dependence on current density of the electroluminescence peak wavelength, showing the reliability of strain-tunable emission at different injection levels. To prevent degradation at high temperatures and to minimize the effect of localized hot spots on device performance, we used a polyimide film with high thermal conductivity, coupled with a Peltier module, to facilitate heat dissipation and to keep a constant temperature during operation. We also maintained a forward current density of less than 20% of the lowest injection level where thermal failure started to take place. When the current density was high, the devices failed sooner, and visible degradation was observed in the channel region. We therefore kept the current levels within the range shown (around  $4 \text{ A}/\text{cm}^2$  to  $90 \text{ A}/\text{cm}^2$ ) and the device showed stable operations over roughly 8 h (see Extended Data Fig. 5d, e). **b**, Distribution of angular intensity of

the strain-tunable bP LED, calculated with finite-difference time domain (FDTD) simulations (FDTD Solutions, Lumerical). Precise computations await further study on changes in the refractive index of bP with strain (compressive and tensile), but here we simply calculated the angular distribution of the bP LED at two different peak wavelengths, using the published refractive indices of bP without strain. **c**, Left, schematic of the device architecture. Right, table showing published<sup>28,47,64–66</sup> complex refractive indices of the polyimide substrate, bP and MoS<sub>2</sub>; these values were used for simulations. We found the angular distributions at two different wavelengths to be close enough that we could assume there was no discrepancy between the power collections at these two emission wavelengths using an objective lens with a fixed collection angle. **d**,  $I$ - $V$  curves of a strain-tunable bP-MoS<sub>2</sub> LED measured at 0.20% of compressive strain and 1.06% of tensile strain.



**Extended Data Fig. 4 | Temperature-dependent performance of strain-tunable bP LED.** **a**, Electroluminescence spectra for the bP LED on a polyimide substrate, operating at a constant current density of  $20 \text{ A cm}^{-2}$  and at different temperatures, under compressive strain (0.2%) or tensile strain (1.0%). **b, c**, Peak wavelength (**b**) and peak intensity (**c**) of the

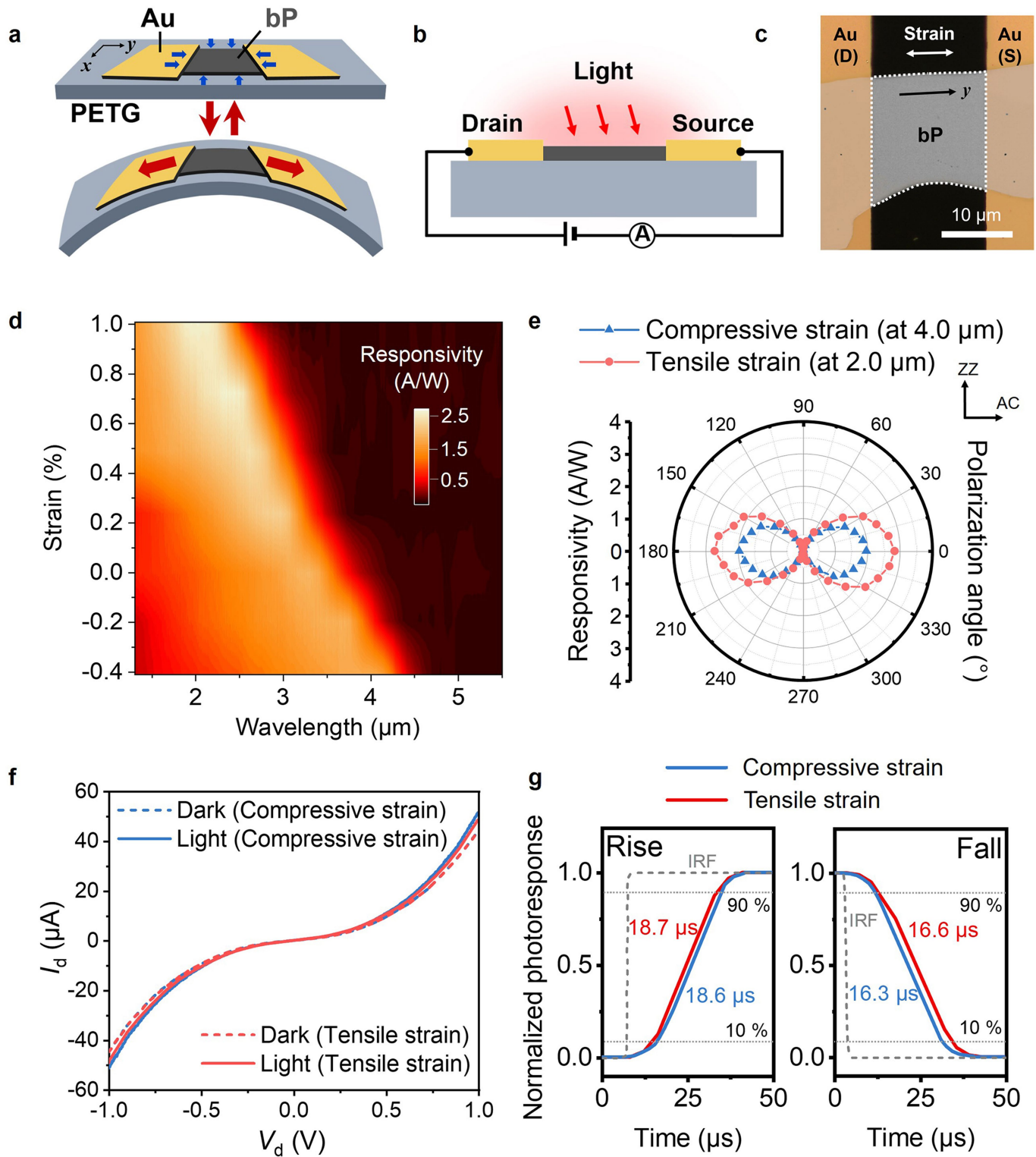
electroluminescence from the bP LED under different strains and at different temperatures. Note that, to achieve heat dissipation and a uniform temperature control during device operation, dry  $\text{N}_2$  gas was consistently purged, and a mechanically flexible heat sink was installed, connected to the cold finger of the cryostat.



**Extended Data Fig. 5 | Tuning emission wavelengths to detect different gases.** **a**, Normalized electroluminescence spectra of bP LED with 0.2% compressive strain, 0.3% tensile strain and 1.0% tensile strain, for detecting CO<sub>2</sub>, CH<sub>4</sub> and H<sub>2</sub>O, respectively. **b, c**, Sensor response from the device under 0.2% compressive strain in the presence of CH<sub>4</sub> gas (**b**) and under 0.3% tensile strain in the presence of CO<sub>2</sub> gas (**c**). Our approach showed minimal CH<sub>4</sub> detection at a concentration of 2.5% under 0.2% compressive strain, and at

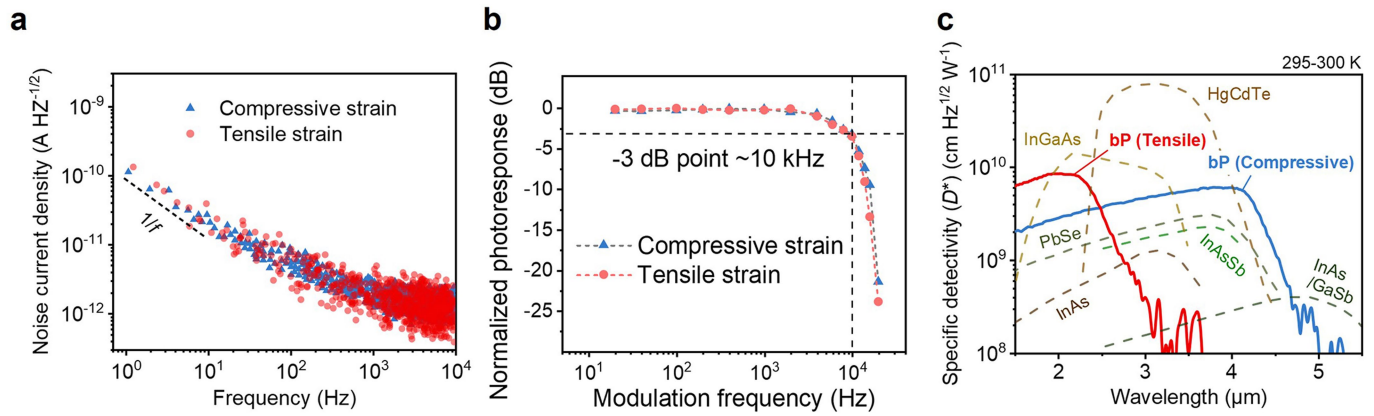
0.3% tensile strain, it could no longer detect CO<sub>2</sub> gas. **d, e**, Stability of the gas-sensing setup for the bP LED measured under 0.2% compressive strain (**d**) and 0.3% tensile strain (**e**). Both measurements were performed at a current density of 20 A cm<sup>-2</sup> with  $f_{mod}=1\text{kHz}$ . Over 8 h of measurement, the device exhibited a maximum drift of 0.90% and 1.22% for 0.2% compressive strain and 0.3% tensile strain, respectively.

# Article



**Extended Data Fig. 6 | Strain-tunable photoconductors based on bP.**  
**a**, Schematic of a strain-tunable bP photoconductor. **b**, Schematic of the device architecture, showing the generation of a photocurrent at a bias voltage. **c**, Optical micrograph of the device. D, drain; S, source. **d**, Strain-dependent spectral photoresponse. A/W, amps/watts. **e**, Polarization-dependent responsivity at 4.0  $\mu\text{m}$  and 2.0  $\mu\text{m}$  for the device under 0.4% compressive strain

and 1.0% tensile strain, respectively. **f**,  $I$ - $V$  curves for the strain-tunable bP photoconductor measured in the dark and under illumination by a 1,000 K black body. **g**, Rise and fall times (between photoresponses of 10% and 90%) under 0.4% compressive and 1.0% tensile strain, using a 1,650-nm laser at roughly 10  $\text{mW cm}^{-2}$ . All measurements were conducted at a bias voltage of 100 mV from a device comprising bP of thickness 22 nm.

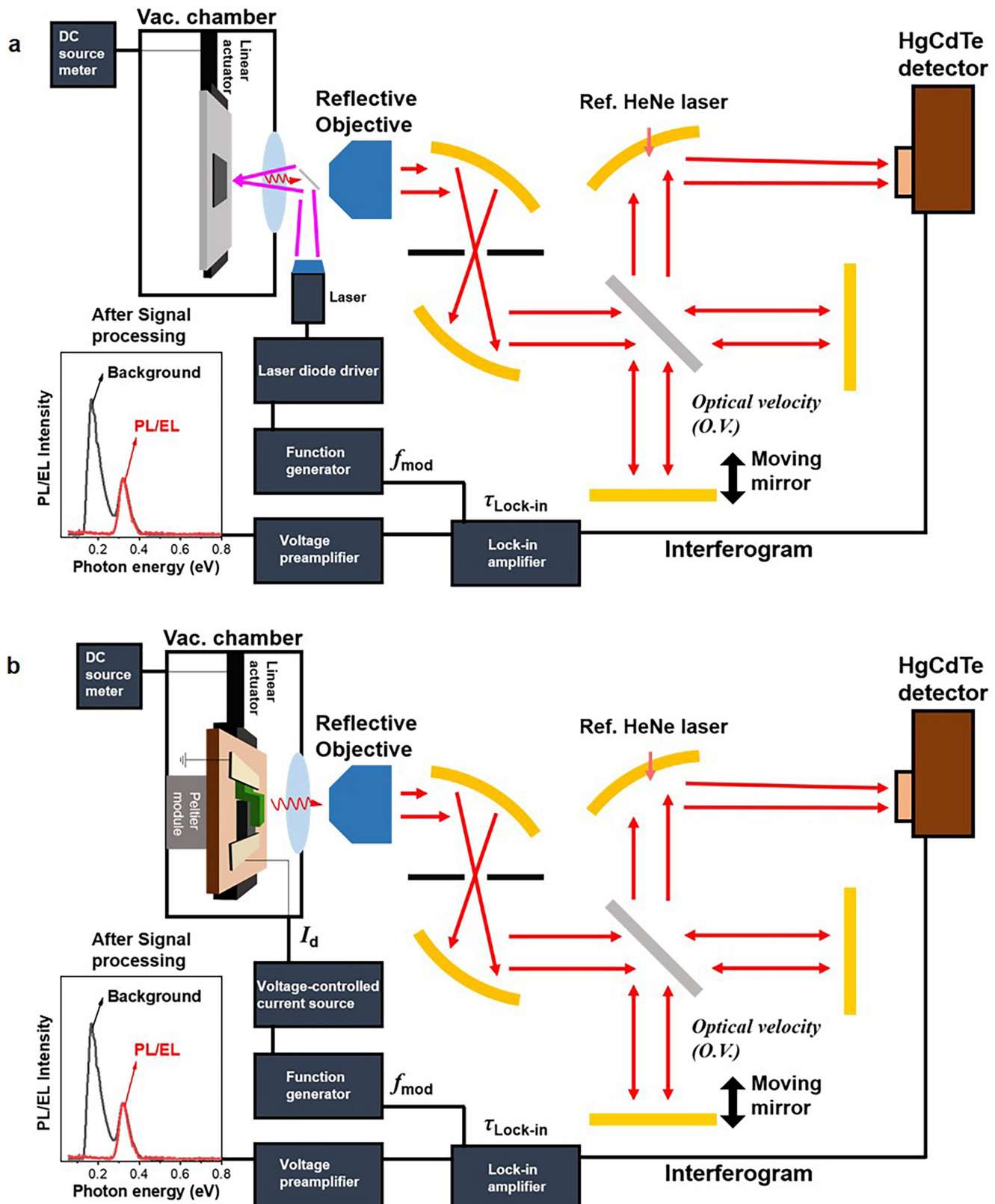


**Extended Data Fig. 7 | Detailed characterization of a variable-spectrum bP photoconductor.** **a**, Spectral noise density under 0.4% compressive and 1.0% tensile strain. The dashed line indicates the  $1/f$  curve at low frequency.

**b**, Normalized photoresponse of the strain-tunable bP photoconductor measured as a function of modulation frequency. The device was measured at a

$V_d = 100 \text{ mV}$  and excited by a 1,650-nm laser, showing a 3-dB frequency of 10 kHz. **c**, Specific detectivity ( $D^*$ ) as a function of wavelength at room temperature, for the bP device with 0.4% compressive and 1.0% tensile strain and for various commercially available photodetectors.

## Article



**Extended Data Fig. 8 | Setups for measuring photoluminescence and electroluminescence.** **a**, The IRPL setup. **b**, The infrared electroluminescence (IREL) setup. For both measurements, the emission from bP was collected by a reflective objective and sent to the external port of the FT-IR spectrometer, with  $f_{\text{mod}} = 5 \text{ kHz}$ ,  $\tau_{\text{Lock-in}} = 300 \mu\text{s}$  and optical velocity =  $0.0633 \text{ cm s}^{-1}$ .

Ref., reference; Vac. chamber, vacuum chamber. The total interferogram from the HgCdTe (MCT) detector and the modulated interferogram from the voltage preamplifier were used to separate the photoluminescence/electroluminescence signal from the thermal background.

**Extended Data Table 1 | Strain-induced bandgap shift of semiconductors in the SWIR/MWIR range**

Material	Bandgap shift rate (meV/%)	Bandgap ( $\varepsilon = 0\%$ ) (eV)	Applied strain		Reference
			Type	Value (%)	
bP	162	0.35	Uniaxial (ZZ)	-0.66 ~ 1.21	<b>This work</b>
InAs	36	0.35	Biaxial	-3.2	[67]
InN	10	0.7	Biaxial	-9.9	[68][69]
Ge	62	0.67	Biaxial	-0.13 ~ 1.78	[26]

The values quoted are from this work and refs.<sup>26,67-69</sup>.

## Article

**Extended Data Table 2 | Parameters used to calculate the theoretical quantum yield from the ABC model**

Material	$n_i$ (cm <sup>-3</sup> )	B (cm <sup>3</sup> /s)	C (cm <sup>6</sup> /s)	References
InAs	$1.0 \times 10^{16}$	$1.1 \times 10^{-10}$	$1.1 \times 10^{-26}$	[70][71]
PbSe	$3.0 \times 10^{16}$	$8.0 \times 10^{-11}$	$1.1 \times 10^{-28}$	[72][73]
GaSb	$9.6 \times 10^{11}$	$3.8 \times 10^{-10}$	$9.3 \times 10^{-28}$	[70][74]
bP (25 nm)	$2.5 \times 10^{15}$	$2.7 \times 10^{-21}$	$4.1 \times 10^{-43}$	[29]

The values quoted are from refs. <sup>29,70-74</sup>.